Dynamic Range Characterisation of Silicon Photomultipliers

von

Tobias Kowalew

Bachelorarbeit in Physik

vorgelegt der

Fakultät für Mathematik, Informatik und Naturwissenschaften
der RWTH Aachen

im Februar 2013

angefertigt im
III. Physikalischen Institut A
RWTH Aachen

Erstgutachter

Prof. Dr. Thomas Hebbeker
III. Physikalisches Institut A
RWTH Aachen

Zweitgutachter

Prof. Dr. Christopher Wiebusch
III. Physikalisches Institut B
RWTH Aachen

Abstract

FAMOUS is a novel fluorescence telescope under development and uses silicon photomultipliers (SiPMs) as light sensitive component. In an SiPM many photodiodes are connected in parallel which provides single photon counting as well as photomultiplier tubes, but with a hinger detection efficiency. To calculate the irradiating photon flux out of the measured flux, precise information on the photon detection efficiency as well as on the dynamic range is needed.

Within this bachelor thesis the dynamic range of different SiPM types is measured. For this purpose a measurement setup is developed providing an irradiation of the SiPM with a well-defined flux of light. A pulsed LED with a peak wavelength of 420 nm is used. This wavelength matches the peak sensitivity of the SiPM. At the end a comparison with a Monte-Carlo based simulation package G4SiPM is carried out to valid one the one hand the understanding of the SiPM working as well as the simulation package itself.

Zusammenfassung

FAMOUS ist ein Floureszenzteleskop in der Entwicklung. Es basiert auf Siliziumphotomultipliern (SiPMs) als optische Komponente. Ein SiPM besteht aus einem Array von einzelnen Photodioden, welche bei einer Betriebsspannung oberhalb der Durchbruchspannung lawinenartig Elektron-Loch-Paare generieren, die einen messbaren Strom erzeugen. Damit man von gemessener Ladung auf die Photonenanzahl schließen kann, muss neben der PDE (Photondetektionseffizienz) auch der Dynamikbereich bekannt sein, da die PDE von der Intensität der Lichtmenge abhängt die auf den SiPM trifft.

Ziel dieser Bachelorarbeit ist es diesen Dynamikbereich verschiedener SiPMs zu vermessen. Dazu wird ein Versuchsaufbau verwendet, der es ermöglicht Anzahl der Photonen bei fester Emissionsdauer zu variieren und gleichzeitig das Signal von SiPM und einer PIN-Diode, die als Referenz genutzt wird, zu speichern. Als Lichtquelle wird eine gepulste LED verwendet, welche eine Peakwellenlänge im UV-Bereich (420 nm) aufweist. Ein Vergleich mit dem Monte-Carlo Simulationsprogramm G4SiPM soll sowohl das Verständins des SiPMs als auch das Simulationsprogramm selbst validieren.

Contents

List of Figures

List of Tables

Outline

Through all ages, people are fascinated by the sky and are trying to find messages coming from outer space. What first began with astrology, passes into astronomy in the age of scientific revolution. More and more people began studying the sky systematically and new inventions arose such as Galileo Galilei's telescope. Despite of all available techniques and knowledge, 400 years later, the number of unresolved issues is still rising.

One branch of current research with a lot of pending questions is dealing with cosmic rays. Cosmic rays are in opposition to its name high energetic particles with an energy range starting with several MeV and ending up with vast rest energies, which can be compared with those of a tennis ball in a single sub atomic particle or nuclei ($\approx 10^{20}\,\mathrm{eV}$). They travel almost with vacuum speed of light and penetrate the atmosphere of the Earth constantly. They are topic of contemporary research. Present-day focus is lying on ultra-high-energy cosmic rays meaning particle energies beyond $10^{18}\,\mathrm{eV}$.

These ultra-high-energy cosmic rays are studied for instance by the Pierre Auger Observatory in the Pampa Amarilla in western Argentina. Using techniques such as Cherenkov light detection or fluorescence spectroscopy, scientists are investigating questions like: What are the sources of cosmic rays? Which acceleration mechanisms exists? What can we learn about those fields and can the investigation of cosmic rays advance the understanding of the universe itself?

A worldwide working group have analysing data since the first data acquisition in 2004. So steady improvement and progress are guaranteed and inevitable, such as a construction of a prototype fluorescence telescope called FAMOUS. The hitherto used photomultiplier tubes as light sensitive components are substituted with silicon photomultipliers, which can provide various benefits in its handling and have a much better detection efficiency for arriving photons than traditional PMTs.

Given that SiPMs are relatively novel devices for light detection, information on its characteristics has still to be acquired. This bachelor thesis aims to characterise the dynamic range of SiPMs with two different cell sizes and a subsequent comparison to a Monte-Carlo model. Such simulations are very important because they provide a simpler and faster way to gain information on the behaviour in a future experiment. But therefore knowledge about robustness of our model and recognition of enhancements are not only very useful, but also of fundamental importance.

This thesis begins with two introduction chapters. The first chapter gives a general overview on cosmic rays and detection techniques. The passage to the second chapter forms a section about the fluorescence telescope called FAMOUS which makes use of the novel silicon photomultipliers. Chapter two deals with semiconductors and their application as photon detectors.

Chapter three illustrates the measurement setup, what kind of devices are used and how they fit together to provide a measuring apparatus which is able to determine the dynamic range of SiPMs. Additionally it deals with calibration of the setup and a short discussion about the used LED as proper light source.

The subsequent chapter four presents the analysis methods as well as a discussion about the feasible operating range for FAMOUS based on dynamic range characterisations. If possible, a validation with other measurements prove its correctness of measurements performed in this thesis. At the end the data are compared with the Monte-Carlo simulation performed with the G4SiPM simulation package.

Chapter 1

Detection of Cosmic Rays

This chapter gives a short overview on cosmic rays and extensive air showers. At the end the novel prototype of a fluorescence telescope is introduced which makes use of silicon photomultipliers. Unless otherwise stated the given information is based on [1] and [4].

1.1 Cosmic Rays

Until 1912, the established idea of ionising radiation assumes the Earth to be the source. Therefore, Viktor F. Hess tried to measure a decreasing ionisation rate as a function of the altitude. He launched a series of balloon flights up to 5350 m altitude. But his discovery was the very opposite, namely an increasing rate above 2500 m. He concluded that the radiation comes from space instead of Earth [2]. Furthermore, he assumed cosmic rays to be electromagnetic in nature. Due to the importance of his discovery and its consequences, he won the Nobel prize in physics in 1936.

Henceforward, many experiments were performed to investigate the novel cosmic rays. During the 1930's, it was proven that cosmic rays are not electromagnetic rays but electrically charged particles. For the following twenty years cosmic rays have been the major source for investigations of subatomic particles.

Today, the chemical composition of the majority of the cosmic rays spectrum is exactly scanned. Only composition of the regime of ultra-high-energy cosmic rays (UHECRs) is still unclear. Cosmic rays with lower energies consist of approximately 88 % protons, 10 % α-particles and 1 % of heavier ionised nuclei. Concerning the ionised nuclei, it was found that they occur in the same relative abundances as in the solar system with at least only exceptions. Just approximately 1 % of cosmic rays are electrons originating from our galaxy.

1.1.1 Energy Spectrum

In recent decades, various experiments on the flux of cosmic rays are carried out. Its spectrum ranges from several MeV up to at least several 10^{20} eV detected by the Fly's Eye experiment [3]. The spectrum of the flux, containing data taken from eleven different experiments, is shown in figure 1.1. For energies greater than 10^{11} eV the flux follows a power law

$$\frac{d^4N}{dEdtd\Omega dA} \propto E^{\gamma} \ , \tag{1.1}$$

as can easily cognised in figure 1.1.

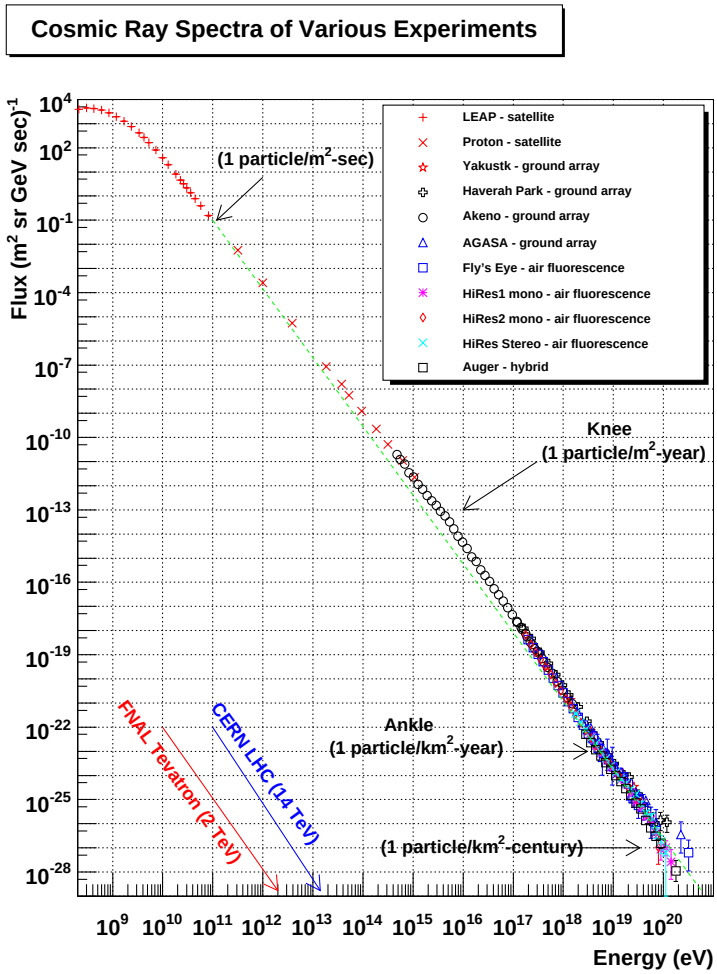

Figure 1.1: Cosmic ray flux as a function of energy containing data from various experiments listed in the legend box. For comparison only, the highest possible energy of the particle accelerators Tevatron and LHC are enlisted. Taken from [3].

The spectral index γ is not a constant over the whole energy regime. Below the so called knee at an energy of $4{\cdot}10^{15}$ eV, the index equals $\gamma = -2.7$ but then increases to $\gamma = -3.1$. A common explanation is that the knee coincides with the "upper energy limit in the acceleration process of galactic supernovae and a leakage of cosmic rays from the galaxy due to a very weak galactic magnetic field ($B \approx 0.3nT$)" [4]. At an energy of E = $4{\cdot}10^{17}eV$, a second knee can be found at which the index changes again to $\gamma = -2.6$ as a reason of a predicted occurrence of heavy nuclei. The last structure is represented by the ankle. The Greisen-Zatsepin-Kuzmin cutoff (GZK-cutoff) may

act as the end of spectrum. At energies beyond 10^{20} eV interactions between cosmic rays and photons of the cosmic microwave background become more probable due to a higher cross section. As a result, energy transfers to the participant photon which leads to a energy loss of the cosmic ray until their energy deceed the GZK-cutoff limit. The different spectral indices can be easily distinguished in figure 1.2, where the flux is multiplied with E^3 on this purpose.

The rate drops from 1 particle m^{-2} sec^{-1} at an energy of 10^{11} eV to 1 particle km^{-2} $century^{-1}$ which can also been seen in figure 1.1. Due to the very rapidly decreasing rate at high energies, a direct investigation of the primary particle is no longer possible and other detection techniques are needed as introduced at the end of the following section.

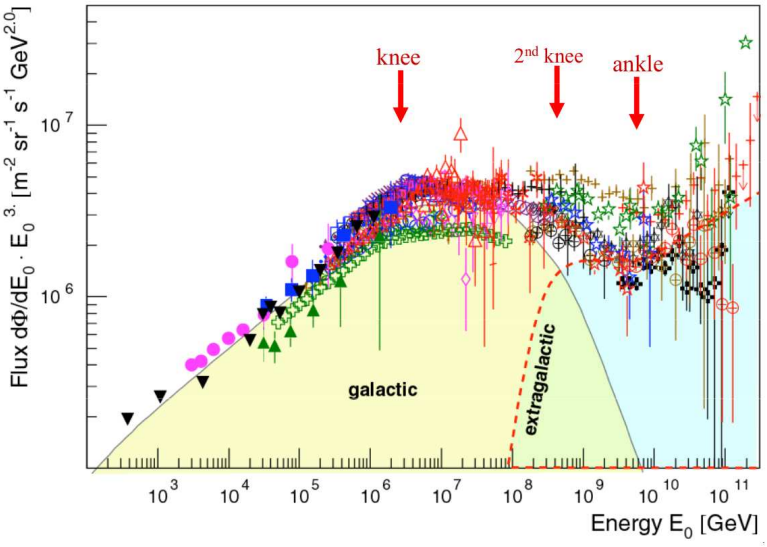

Figure 1.2: Flux multiplied with E^3 to emphasise the various spectral indices (an index of 3.0 represents a horizontal line). Additionally the assumed regimes of galactic and extra galactic sources are denoted by coloured areas [10].

1.2 Extensive Air Showers

In 1938 Pierre Auger noticed that two detectors located several meters apart from each other measured exactly the same arrival time of particles. Auger calculated the energy of the primary particle to be in the order of 10^{15} eV [5]. After carrying out more precise measurements with an array of detectors covering an area of 25 m^2, he concluded that the time coincidence is the result of a single primary particle [6]. This was the discovery of extensive air showers (EASs).

It is known that EASs are induced by cosmic rays entering the atmosphere and their interaction with air molecules at an altitude of approximately a few tens of kilometres. The secondary particles of the interaction induce themselves new cascades. So a massive growth is initialised and continues as long as the energy of the generated particles are able to compensate the ionisation energy. At the balance point, the

avalanche has reached its maximum and new particles are not created any longer. The balance point is referred to the shower maximum $X_{\max}$ and is a measurement of elementary importance because it enables to draw inferences to the energy of the primary particle [7].

The resulting avalanche, sketched up in figure 1.3, forms a front comparable to a thin disk with a small spherical bulge. The disk is only a few metres thick and travels nearly with the vacuum speed of light towards ground. Since this exceeds the speed of light in the atmosphere, the nett polarisation of the air leads to ultraviolet Cherenkov light. This process produces 10 to 20 Cherenkov photons per particle and traversed meter of the atmosphere. Since the number of charged particles in the shower is at least 10^8 near X_{max}, Cherenkov radiation is detectable by telescopes which are sensitive in the ultraviolet range. Furthermore, on the way through the atmosphere, nitrogen molecules are excited and so emit fluorescence light which leads to a weak tracer that can be observed using optical telescopes [10], [11]. Both Cherenkov light and fluorescence light are radiation of interest in the Pierre Auger Observatory.

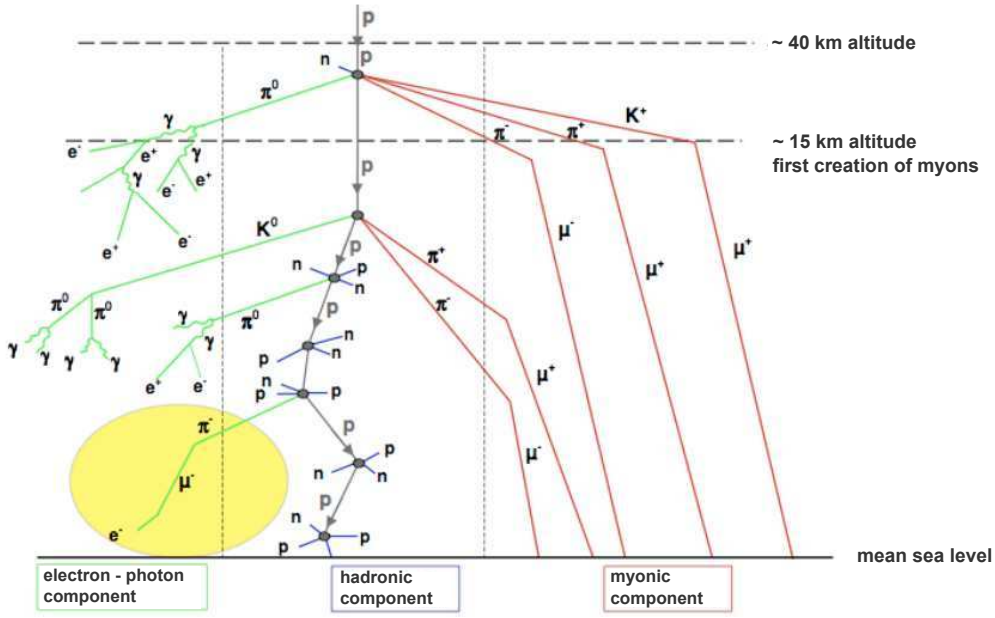

Figure 1.3: Schematic diagram showing the shower development and the electromagnetic, hadronic and muonic component. The shaded area denotes the possibility of transitions between the components. Adapted from [9].

1.3 FAMOUS

The "**F**irst **A**uger **M**ulti-pixel-photon-counter-camera for the **O**bservation of **U**ltra-high-energy-cosmic-ray air **S**howers" (FAMOUS) is a small prototype fluorescence telescope which may be a possible successor for present used fluorescence telescopes. The telescope has a refractive design consisting of a Fresnel lens with a diameter of

502 mm. In the focal plane, which has a distance of 502 mm from the Fresnel lens, novel silicon photmultipliers (SiPMs) are deployed instead of common photomultiplier tubes (PMTs). The final version of FAMOUS will consist of 64 pixels. Due to the higher photon detection efficiency (PDE) of SiPMs in contrast to PMTs, the sensitivity gets increased allowing to detect more distant and lower energy showers. Since the chemical composition of UHECRs are still not completely investigated in consequence of the very low flux for energies beyond 10^{18} eV, FAMOUS might contribute to an increase of the current understanding of the chemical composition as well as of the development of EAS [4].

Chapter 2

Silicon Photomultiplier

As the previous chapter explained the requirement for light sensitive devices even with the efficiency of single photon detection, this chapter outlines a novel device for its detection and its functional principle. Since RCA developed the first single stage commercial photomultiplier tube (PMT) in 1935, they became expeditiously the main device for the detection of very low light fluxes used by both astrophysicists and particle physicists. However, there are several fields of application they are inapplicable for. Such as those where small-sized devices are required. Common PMTs have a diameter of a few centimetres and a length greater than 10 cm. Furthermore, they need supply voltages in the order of $\approx 1\,\mathrm{kV}$ and they are sensitive to magnetic fields. Hence other techniques and models are required which can be satisfied by semiconductor technology.

2.1 P-N Junction

Semiconductors are solids which form a fluent passage between conductors and insulators. At absolute zero, they act as insulator, but an energy gap E_G ($\widehat{=}$ difference between valence and conduction band) of several eV allows electrons to be thermally excited from the valance into the conduction band. This temperature dependent conductivity can be raised by doping. Elements of the III (p-doped) or V (n-doped) main group can either provides holes, which can be occupied by electrons more energy-efficient, or allocate further electrons of a superior valance band, so they can excited more easily to the conduction band.

If a p- and n-doped semiconductor are connected, as sketched up on the left in figure 2.1, the Fermi energies of both regions assimilate each other. Due to the abrupt change of the concentration of the charge carriers and until equilibrium is reached, electrons drift into the p-region and holes into the n-region creating a depletion layer around the junction. This separation of charge causes an electric field which in turn leads to a built-in potential as graphed in figure 2.1 downright.

Theoretically, a p-n junction can already be used to detect single photons. If a semiconductor is irradiated with photons of an energy $\hbar\omega > E_G$, their absorption lifts the electrons into the condition band leaving holes in the valence band. The created electron hole pairs (eh-pairs) contribute to the current flow. In case of silicon this minor effect is not measurable using ampere-meters [13]. Therefore an intrinsic amplification is required to generate a higher current flux.

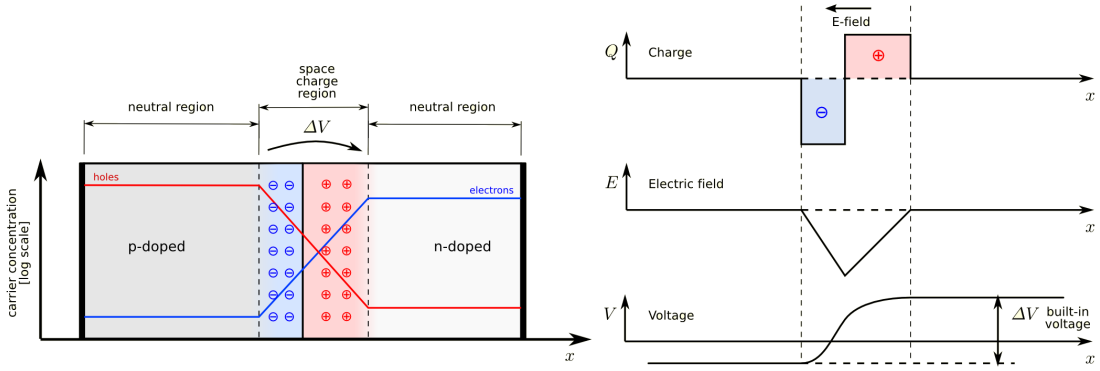

Figure 2.1: Left: sketch of a p-n junction in thermal equilibrium including the log scaled number of electron and holes. Right: quantitative charge distribution Q, electrical field E and built-in voltage along a p-n junction.

2.2 Avalanche Photo Diodes

To achieve the previously mentioned intrinsic amplification, a p-n junction has to be modified as shown in figure 2.2. A low resistivity silicon layer is topped by an epitaxial grown, low doped silicon. Thereover ranges a p-n junction created via diffusion and ion implantation. The supreme layer of the p region gets highly doped to ensure a safe electric contact. Applying a reverse bias voltage V_{bias}, which has to be extremely close to the breakdown voltage V_{break}, enlarges the potential difference ΔV between the p- and n-layer. Hence the electric field strength is increased.

For a high electric field $E > 2.5 \cdot 10^5\,\text{V cm}^{-1}$ between the p- and n-zone, an incoming photon can create an eh-pair. Both the electron and the hole undergo high acceleration and their gained energy is sufficient to produce further eh-pairs. So an avalanche is launched in the area of the p-n junction until multiplication stops as soon as charge carriers reach the low field area of the p-layer. The avalanche travels through the specific n-zones to an electric contact where a signal with a gain in the order of 10^2 can be tapped. This gain can only be provided if the photoelectron is created near the depletion zone of the pn-junction. Otherwise only a smaller part of the electric field contribute to the acceleration leading to a reduced amplification. Accordingly highest gains are achievable for wavelengths $\lambda \lesssim 500\,nm$ because the penetration depth increases with energy. For wavelengths $\lambda > 500\,nm$, the position of first inaction mismatches the optimum and the gain is smaller.

By increasing V_{bias} the operation mode of the APD changes from the linear mode into the Geiger-mode. In contrast to the linear mode, additional initiations of secondary avalanches are started by holes or secondary photons. The self-sustaining avalanche process has to be quenched by a high-ohmic resistor or an active quenching circuit providing a signal with an invariable amplitude. The signal of G-APDs are amplified by a factor $10^5 - 10^7$, but also gains of 10^4 are available. Because a single photon generates a signal of several millivolts on a $50\,\Omega$ load, single photon detection is possible. The gain G of the G-APD is proportional to $G \sim A \sim C \cdot (V_{\text{bias}} - V_{\text{break}})$.

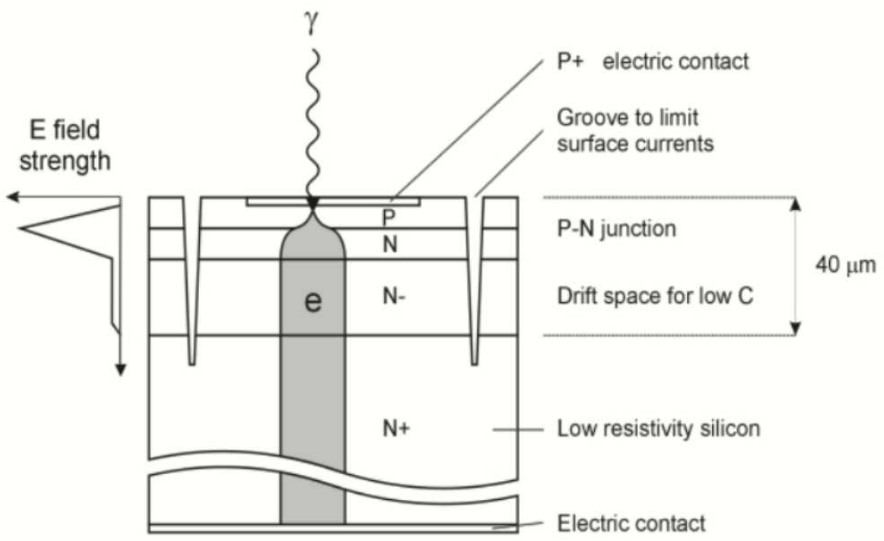

Figure 2.2: Schematic layout of an Hamamatsu S8148 avalanche photo diode (APD). The trigger probability is maximal at the bottom edge of the depletion zone. A reverse bias voltage is applied on the electric contacts to provide a high electric field [14].

A represents the amplitude of the signal, C the capacitance, V_{bias} the operating bias voltage, and V_{break} equals the breakdown voltage. The difference between bias voltage and breakdown voltage is defined as the overvoltage $V_{\text{over}} = V_{\text{bias}} - V_{\text{break}}$.

2.3 Silicon Photomultiplier

A single G-APD is ineligible if a signal proportional to the incoming photon flux is required. But if many G-APDs are connected in parallel, the requested proportionality is hereby assigned. So an array of G-APDs is created whereas one G-APD refers to one cell. Each cell can be represented by a capacity and the quenching resistor in an equivalent circuit diagram [15]. Additionally each cell triggered separately by a single photon which enables the detection of photon numbers close to the number of cells. The proportionality is ensured because every photon triggers one cell as long as only few cells are triggered. After a cell fired, a characteristic recovery time $\tau_{\text{rec}} \sim C \cdot R_{\text{Q}}$ is needed until the cell is fully loaded again. Before this time is elapsed a breakdown produces only a signal with an amplitude smaller than the standard height. An exponential recovery behaviour has been verified in [16] with a time constant of a few tens of nanoseconds:

$$G \sim V_{\text{over}} \sim V_{\text{bias}} \left(1 - \exp^{-\frac{t}{\tau}}\right) \tag{2.1}$$

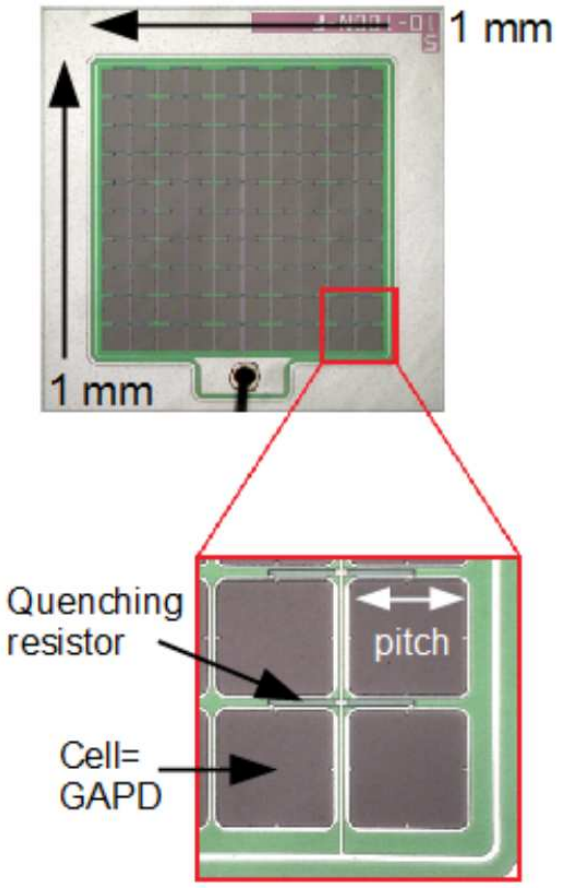

Figure 2.3: Close-up image of a Hamamatsu SiPM consisting of 100 cells ($1 \times 1\,\mathrm{mm}^2$; $100\,\mu$m pixel size). Adapted from [22].

2.3.1 Noise Phenomena

A fired cell is not invariably referable to an incoming photon. There are several noise effects pretending an absorbed photon. Because these effects enlarge the measured number of photons, it is inevitable to take them into account. Measurements of these effects can be found in [23]. Figure 2.4 gives an overview about all noise phenomena and the gain as a function of the overvoltage.

2.3.1.1 Thermal Noise

Thermal excitation can generate an eh-pair which is able to induce an avalanche. A typical noise rate of an SiPM cell is in the order of magnitude of 10 kHz at room temperature. A temperature drop of eight degrees decreases the noise rate by a factor of two. Since the noise rate is proportional to the number of cells, the rate of a whole SiPM can easily exceed a few MHz.

2.3.1.2 Optical Crosstalk

If an eh-pair created during an avalanche recombines, a photon will be emitted which in turn is able to start a new avalanche in a neighbouring cell. On the one hand the

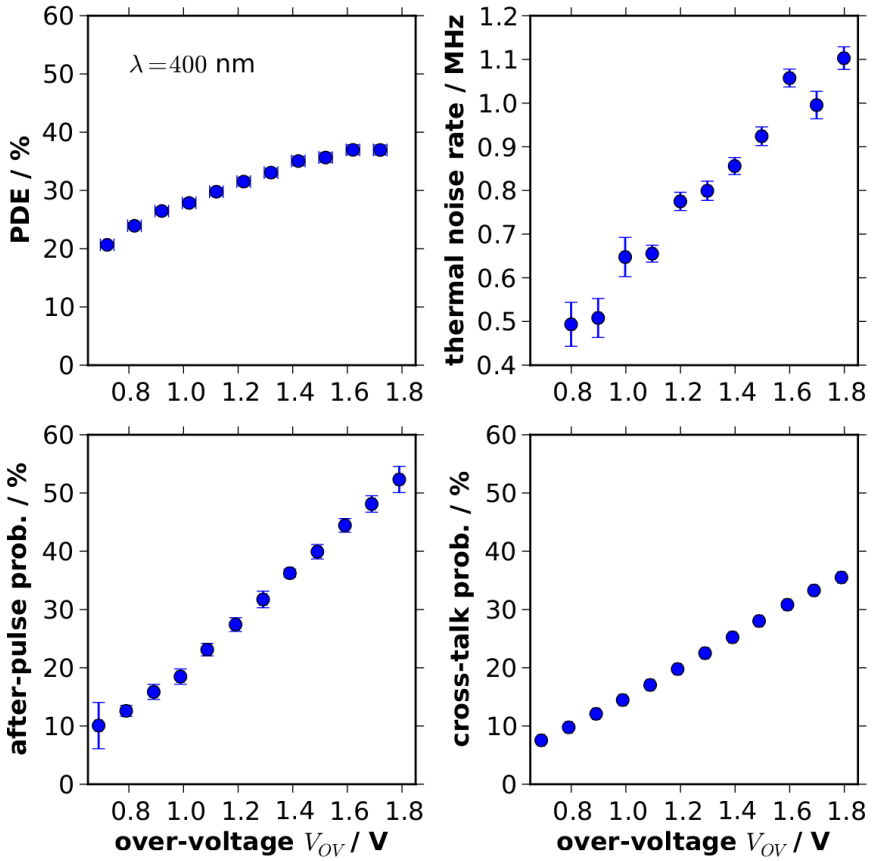

Figure 2.4: Roundup of noise phenomena and PDE as a function of the overvoltage. Values recorded of an SiPM with 100 cells out of the S10361 series manufactured by Hamamastu, for a wavelength of $\lambda = 400\,\text{nm}$ and for an ambient temperature of 25 °C. Adapted from [17].

photon can transmit directly into another cell or can first be reflected on the coating. On the other hand the photon can enter the n-substrate of another cell creating a new eh-pair there which can drift into the avalanche region causing a breakdown. The crosstalk probability depends on both temperature and strongly on overvoltage and ranges from 5 % to 35 % for a Hamamatsu SiPM of the S10361 series.

2.3.1.3 Afterpulses

Charge carriers from an avalanche can be trapped by impurities of the silicon. After a few tens of nanoseconds, their release can induce a cell breakdown. Here, too, the probability is strongly overvoltage dependant and varies from 5 % to almost 50 % for a Hamamatsu SiPM of the S10361 series.

2.3.2 Photon Detection Efficiency

An important benefit compared to common PMTs is the higher photon detection efficiency (PDE) of an SiPM. The PDE can be calculated via

$$PDE(\lambda) = \epsilon_{\text{geom}} \cdot \epsilon_{\text{trigger}} \cdot QE(\lambda) \ . \tag{2.2}$$

The geometrical fillfactor ϵ_{geom} is given by the ratio of the active area to the total area of an SiPM. This factor arises from the quenching resistor and the necessary electrical separation between cells. Due to the high electric field strength of the depletion zone in the Geiger-mode, the trigger probability $\epsilon_{\text{trigger}}$ converges fast to $\epsilon_{\text{trigger}} = 1$ for photons with the peak sensitivity wavelength. These two parameters are uninfluenceable and the remaining quantity which can change the PDE is the quantum efficiency. The quantum efficiency represents the probability of an photon illuminating on the active area to initiate an avalanche. Manufacturer specifications sometimes advertise PDEs of over 70 %, but they are overestimated due to noise phenomena.

Chapter 3

Measurement Setup

This chapter introduces the measurement setup. Information on the used devices are given as well as how they work together. The fundamental idea is to illuminate the SiPM with a well-defined flux of light measured by a reference PIN diode which enables a comparison between input and output. The whole measurement is housed in a dark box to shield the setup from ambient light sources. A photograph of the devices housing in a dark box can be seen in figure 3.1 and figure 3.2 shows the schematic layout of the setup.

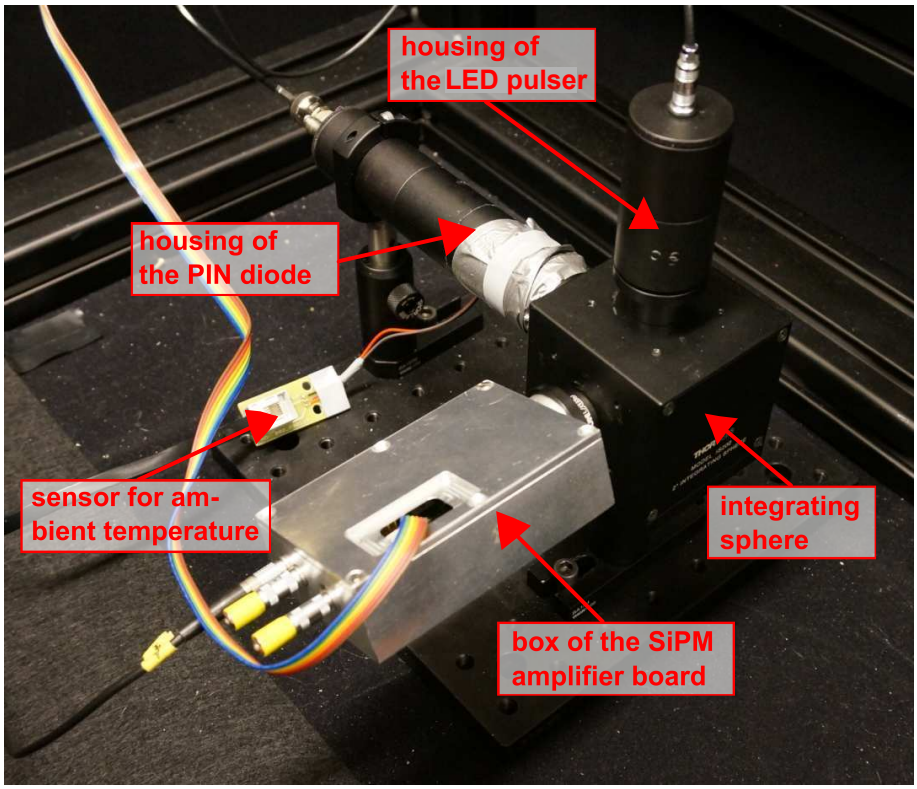

Figure 3.1: Photograph of the measurement setup. The LED pulser, SiPM and PIN diode are connected to the central integrating sphere. Temperature monitoring enables to validate if temperature was constant during a measurement. Picture is taken inside the dark box.

3.1 Idea and Principle

The central point of the setup is formed by an integrating sphere which has four exit ports for light. The sphere diffuses all incoming light and splits it equally to all ports. Furthermore, small tubes are mounted between the exit port and other devices. This ensures that no light can leave the sphere without being reflected at least one time. If necessary, the tubes can be changed by neutral density filters[1] with the same dimensions. Replacing the tube between SiPM and integrating sphere by a neutral density filter reduces the light flux on the SiPM. So it is possible to provide low fluxes on the SiPM as well as higher fluxes on the PIN diode to create a larger current. As a result, the current measured by the picoammeter has a very small uncertainty. The damping factor of the neutral density filter is taken into account by a calibration factor which represents the ratio between the flux on SiPM and PIN diode.

All attached components are housed in their own metal box to eliminate electrical pulses which might distort signals. The boxes are custom-made by the mechanical workshop of III. Physikalisches Institut A, RWTH Aachen. Care has to be taken that SiPM and PIN diode have not to be mounted on the opposite site to prevent reflections from metal surfaces and that the light detectors are placed at the same distance from the centre of the sphere. By keeping the distance constant, the flux per area on SiPM and PIN diode is the same. So the flux on the SiPM Φ_{SiPM} is proportional to the flux on the PIN diode Φ_{PIN} and can be calculated via

$$\Phi_{\mathrm{SiPM}} = \frac{1}{R} \cdot \Phi_{\mathrm{PIN}} \ , \tag{3.1}$$

whereby R is the calibration factor. The PIN diode is driven without a bias voltage so that the current is directly proportional to the detected photon flux. Connecting it to the picoammeter via an high-grade shielded BNC cable minimises current leaks. The mountings of SiPM and PIN diode enable a placement of an aperture in front of them and guarantee that both detectors and aperture are centred. A diameter of 0.5 mm of the aperture covers most of the detector area and only a small part is illuminated, which is important for calibration measurements.

Calibration measurements are needed to convert the current of the PIN diode into photons irradiating on the SiPM. They include four different steps. The current of the PIN diode is measured with and without the aperture in front of the PIN diode. The same is done for the charge dropped by the SiPM. If a neutral density filter was used, the density filter was mounted during the two charge measurements with the SiPM and the current measurement when the aperture was mounted in front of the PIN diode. The measurements using the aperture procure that both SiPM and PIN diode see exactly the same number of photons. Hence two ratios can be calculated whose product forms the correction factor to determine the number of

[1] Absorptive ND Filters; Series NEK manufactured by Thorlabs; optical densities specified at 633 nm.

photons hitting the SiPM out of the current of the PIN diode. The SiPM response is directly amplified by the Beissel amplifier board produced and designed in Aachen. Before the signal is analysed by the QDC, it gets looped through a fan-in/fan-out to reduce the baseline of the response to voltages about $V = -50\,\mathrm{mV}$, as the QDC can only integrate over negative signals. Additionally the fan-in/fan-out allows to split the signal and so monitoring by an oscilloscope. Both, QDC and fan-in/fan-out are mounted in a crate which provides communication via a VMEbus system. The controlling electronics for the amplifier board is housed in the crate too. A connection to the measurement laptop is established by a Wiener VM USB module. The measurement is controlled by a self written C++ program and uses the device library 'LibLAB', developed at III. Physikalisches Institut B, RWTH Aachen, to communicate with the measuring instruments.

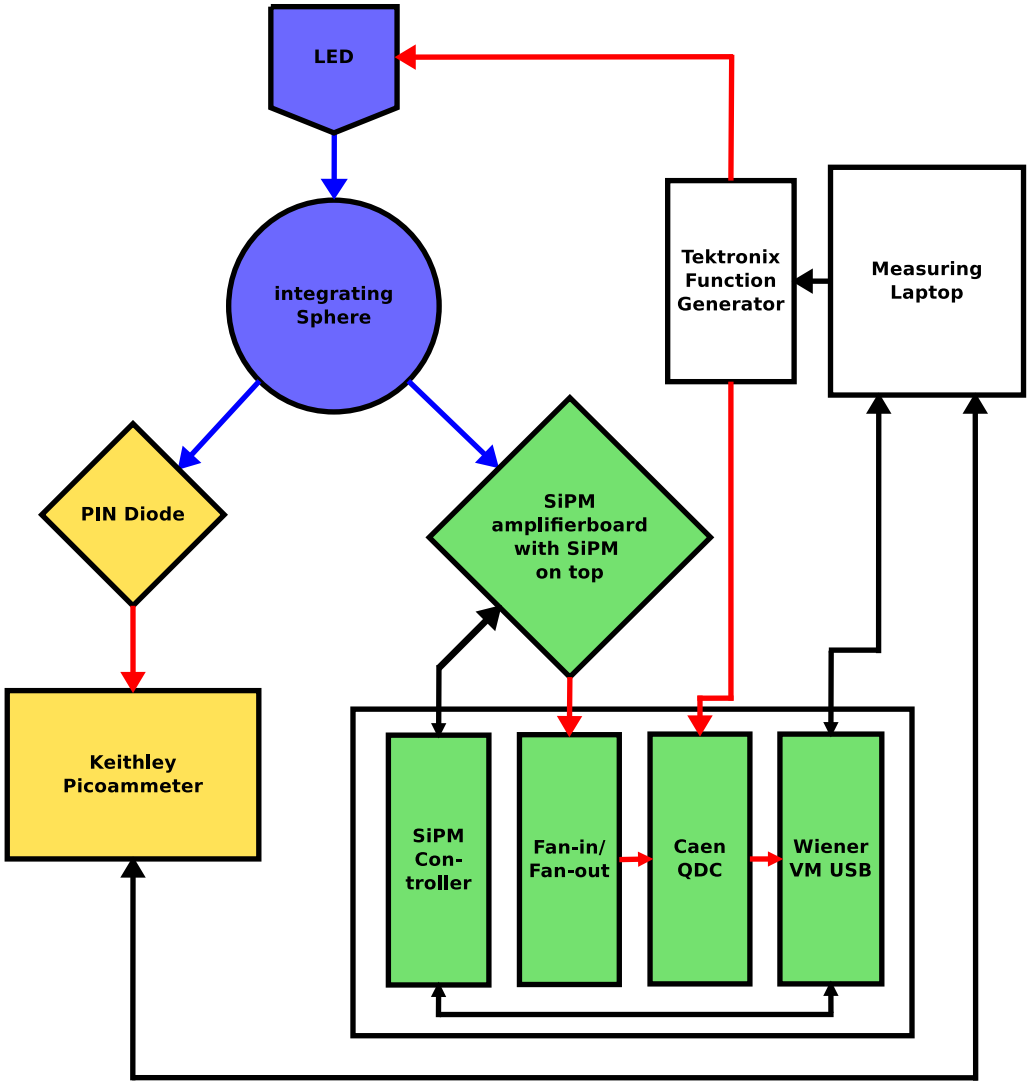

Figure 3.2: Schematic layout of the measurement setup. Signals are red-coloured, light ways blue and data connections black. Devices for the SiPM signal processing are green and the ones for reference measurement of the light flux is yellow.

3.2 Compontens

3.2.1 Amplifier board

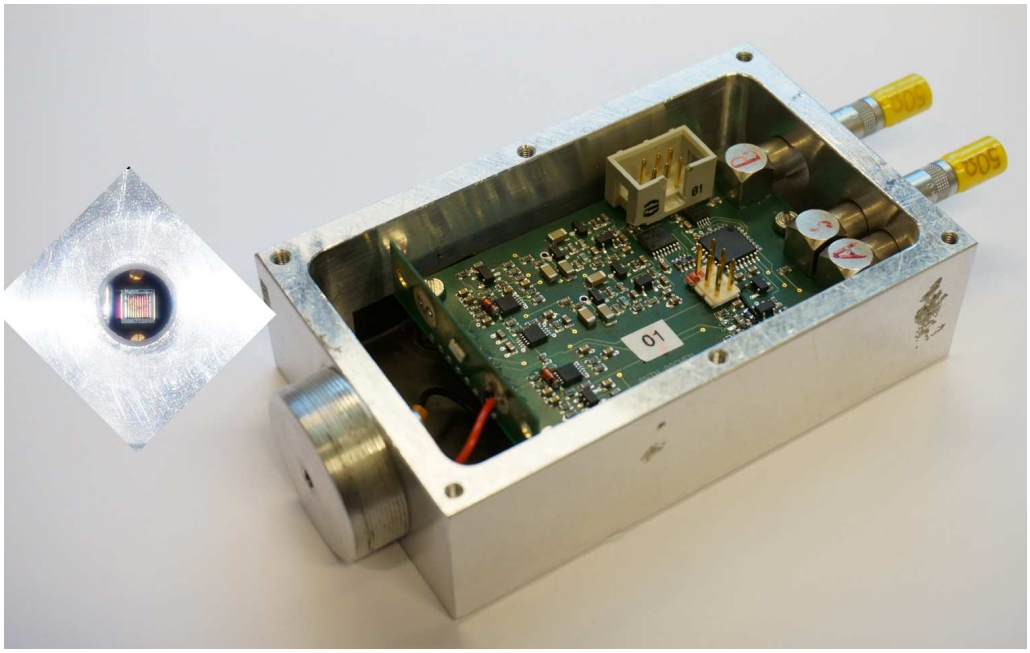

Figure 3.3: Beissel amplifier in its box. On the left a enlarged picture of the SiPM in its mounting is shown.

The used amplifier board was designed and produced at III. Phys. Inst. B, RWTH Aachen University by F. Beissel et. al. in 2011. It provides two equally units which enables to process responses of two SiPMs. A temperature sensor close to the SiPMs connection point can be used to adjust properly the bias voltage against temperature variations with a resolution of 0.1 °C. The only interest of temperature measurements is to keep the gain constant. Additionally the amplifier board acts as an power supply for the SiPM providing bias voltages in a range between 0 V and 80 V with increments of 0.05 V. This is sufficient regarding the temperature progression coefficient of 56 mV K^{-1} of the SiPMs. A typical breakdown voltage of Hamamatsu SiPM is $V_{\text{break}} \approx 70$ V at an ambient temperature of 25 °C. The output amplitude of the amplifier is limited to 1.5 V. A photograph of the board housing in its metal box and connected to the SiPM is shown in figure 3.3.

3.2.2 Characterised SiPMs

The SiPMs employed in FAMOUS are manufactured by Hamamatsu Photonics. Both, the S10361 series as well as the S10958 series provide the UV/blue sensitivity needed for detection of fluorescence light. The S10361 series covers two different sizes ($1 \times 1\,\text{mm}^2$ and $3 \times 3\,\text{mm}^2$) available each with three different pitch sizes (25 μm, 50 μm and 100 μm). Hence the number of cells varies from 100 to 14400. For FAMOUS, an $6 \times 6\,\text{mm}^2$ SiPM out of the S10958 series with a cell pitch size of

100 μm and 3600 cells in total is selected due to the large number of cells and large sensitive area. Due to the limitations of the amplifier board it was only possible to characterise two SiPM with numbers of cells of 100 and 400 because if more than 400 cells are triggered either the signal exceed the 5 V limit or, at lower over voltages, individual peaks can not be resolved anymore. The SiPM applied in FAMOUS is composed of four $3 \times 3\,\mathrm{mm}^2$ SiPM of the S10361 series. Thus, the focus of this thesis lies on the characterisation of the same series. The characterised SiPMs and their specifications given by the manufacturer can be extracted from table 3.1. Figure 3.4 shows a photograph of an SiPM consisting of 100 cells.

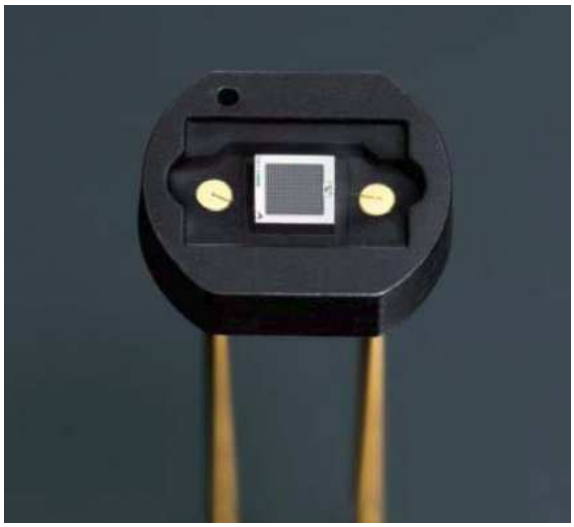

Figure 3.4: Photograph of an $1 \times 1\,\mathrm{mm}^2$ SiPM with a cell size of 100 μm.

The PDE at peak sensitivity drops for smaller pitch sizes mainly due to the reducing active area. Furthermore, a smaller active area results in a lower dark count rate. Since the SiPM response strongly depends on the bias voltage and the breakdown voltage varies from SiPM to SiPM, a precise measurement of the breakdown voltage, done before every measurement, allows to choose the right bias voltage.

3.2.3 PIN Diode and Picoammeter

The Hamamatsu FDS100 Si Photodiode is a silicon based light detector with a quadratic active area of $13\,\mathrm{mm}^2$. It provides a quantum efficiency of approximately 28 % for light with a wavelength of 420 nm which exactly matches the peak wavelength of the used LED [19], [20]. Current measurements of the PIN diode are performed with the Keithley Picoammter 6485, which is a high resolution bus-programmable (RS-232 and IEEE-488) picoammeter. Eight different sensitivity ranges from 20 mA down to 2 nA are available for measurements. Various built in self tests ensure the measured current to be the real current and not to be distorted by an offset. Care has to be taken that all devices have to be connected before running the self tests. The best signal-to-noise ratio is reached for an integration time of 100 ms. Connected via USB to the measuring laptop, the readout is done

Type	S10361-11-100C	S10361-11-400C
Number of cells	100	400
Active Area	78.5%	61.5%
pitch size	$100 \times 100\,\mu\text{m}^2$	$50 \times 50\,\mu\text{m}^2$
Peak sensitivity at [nm]	440	440
PDE at peak sensitivity	65%	50%
Bias voltage	$\approx 70\,\text{V}$	$\approx 70\,\text{V}$
Typ. dark count rate	0.6 MHz	0.4 MHz
Gain	$2.5 \cdot 10^5$	$7.5 \cdot 10^5$

Table 3.1: Manufacturer specifications of the different characterised SiPM types. Values are for an ambient temperature of 25 °C. The PDE is not corrected by crosstalk and afterpulses. [18]

by the LibLAB library developed at III. Phys. Inst. A and III. Phys. Inst. B which provides easy access to common laboratory hardware.

3.2.4 QDC

The Caen V965 is a 12 bit charge-to-digital converter (QDC) equipped with 16 channels with current integrating negative inputs with 50 Ω input impedance. After the input signal is converted to a voltage level by a charge-to-amplitude converter (QAC), the QAC output will be transformed by two analogue-to-digital converters (ADCs) in parallel. One ADC is preceded by a $x8$ gain stage, providing a measurement range from 0 pC to 100 pC. The other one with a $x1$ gain stage allowing measurements ranging from 0 pC to 900 pC. The $x8$ high gain channels have a resolution of 25 fC, while the low gain channels can only resolve 100 fC. Since the input signal must not exceed +15 mV, a linear fan-in/fan-out reduced the baseline of the SiPM signal to −50 mV. A measurement is triggered via an external NIM signal produced by an arbitrary function generator. After an input lag of 15 ns the QDC starts the integration as long as the gate width t_{gate} [21].

3.2.5 Function Generator

Both, the trigger pulses and the LED pulses are generated by the arbitrary function generator AFG3252 manufactured by Tektronix. Two separate output channels can provide signals with an amplitude of 5 V and frequencies up to 240 MHz. A time delay can be used to ensure time coincidence between the trigger signal and the SiPM signal before an analysis via the QDC. Furthermore it is possible to control and to set the parameters of each channel separately. The AFG is connected to the measuring laptop via USB and gets controlled via a self-written Python script.

3.3 Number of Photons in a LED flash

A pulsed Conrad UV-LED 5004PCH02 is deployed as light source because its peak wavelength of 420 nm matches almost perfectly the peak sensitivity of the SiPM at

440 nm and is comparable to the wavelengths of the fluorescence light spectrum. The full width at half maximum amounts to about 20 nm [20]. The LED is pulsed by the function generator with rectangular coils with a pulse width of $t_{\text{pulse}} = 6\,\text{ns}$. The baseline of the pulse is set to $-0.5\,\text{V}$ so that the LED is operated reverse-biased to erase possible afterglow. By varying the amplitude of the pulse, the number of photons can be adjusted. The LED is housed in a tube with a diameter of 30 mm and is attached to a small board with a $50\,\Omega$ resistor which helps to damp oscillations in the supply cable. The tube is screwed onto the top of the integrating sphere, so that all entering light is directioned downwards.

To determine the number of photons N illuminating the SiPM, the current I of a PIN diode is measured by the picoammeter. The number of photons N can be calculated via the formula

$$N = \frac{I}{QE(\lambda) \cdot e \cdot f \cdot R} \,. \tag{3.2}$$

Since the picoammeter provides an internal zero check, it was not necessary to measure a dark current which has to be subtracted from each current value. Dividing the mean current by the electric charge e and the quantum efficiency $QE(\lambda)$ of the PIN diode, the number of photons reaching the sensitive area of the PIN diode per second is obtained. A further division by the frequency f of the pulser results in the number of photons per pulse. To get number of photons irradiating the active area of the SiPM per pulse an additional division by the correction factor R has to be executed. The determination of this correction factor is described in the next chapter.

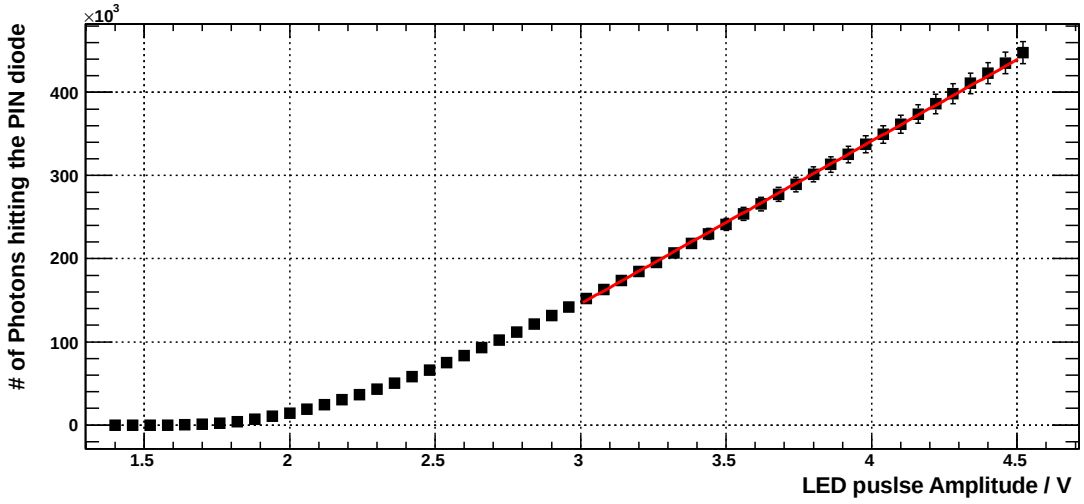

Figure 3.5: Number of photons hitting a 13mm^2 PIN diode per pulse as function of the LED pulse amplitude. The pulse length is $t_{\text{pulse}} = 6\,\text{ns}$.

Figure 3.5 shows the number of photons N reaching the $13\,\mathrm{mm}^2$ PIN diode as a function of the LED pulse amplitude. N can be calculated via the formula above by setting the correction factor R to 1. The uncertainties results from Gaussian error propagation of I, $QE(\lambda)$ and R. The major contributions to the uncertainties arise from σ_R and $\sigma_{\mathrm{QE}(\lambda)}$, which is given by the manufacturer as $\sigma_{\mathrm{QE}(\lambda)} = 0.03 \cdot QE(\lambda)$.

Close to an amplitude of $V_{\mathrm{LED}} = 1.5\,V$, the LED starts emitting photons. The number of photons then increases almost exponentially until from $V_{\mathrm{LED}} \approx 3\,V$ on the number of emitted photons is proportional to V_{LED}. Due to this proportionality it is probable to exclude afterglow at high V_{LED} but it is not exactly verifiable. Since V_{LED} is adjustable with an precision of $\Delta V_{\mathrm{LED}} = 1\,\mathrm{mV}$, the number of emitted photons can be controlled very accurately. Furthermore, the number of emitted photons depends on the temperature of the LED. But the temperature is assumed to be constant during a measurement because temperature variations are smaller than the accuracy of the temperature sensor. This enables the LED to emit always the same number of photons and to preset them.

3.4 Measurement Procedure

A flowchart of the whole measurement procedure can be found in figure 3.6. Each measurement starts with the determination of the breakdown voltage. For this purpose the setup shown in figure 3.2 is used. A photograph of the setup is shown in figure 3.1. At different bias voltages above the breakdown voltage, the gain is determined as difference between the pedestal and the one photon equivalent peak. Drawn up in a graph versus the bias voltage, the breakdown voltage is represented by the intercept with the x-axis. Such a linear regression can be found in figure 4.3 on page 28.

Afterwards calibration measurements are performed: the first step includes taking 100k QDC values at a LED pulse amplitude of 2 V with the neutral density filter mounted in front of the SiPM. In the second step, an aperture with a diameter of 0.5 mm is additionally mounted in front of the SiPM and again 100k QDC values are taken. Calculating the ratio of the mean charge dropped by the SiPM with the aperture in front and of the mean charge measured without the aperture, obtains the first factor of the correction factor. Now the amplitude of the LED pulse has been raised to 4.5 V to determine the second factor. 100 current values are taken by the picoammeter. For the last step, the SiPM and the PIN diode are interchanged and the neutral density filter and the aperture are mounted in front of the PIN diode which ensures that the PIN diode is illuminated with exactly the same light flux as the SiPM with the aperture in front. The tube which had connected the PIN diode with the integrating sphere connects now the SiPM and the integrating sphere, so that same distances are provided. Again 100 current values are taken and the calibration factor R can be calculated. Both calibration measurements and determination of the breakdown voltage are performed before and after each dynamic range measurement.

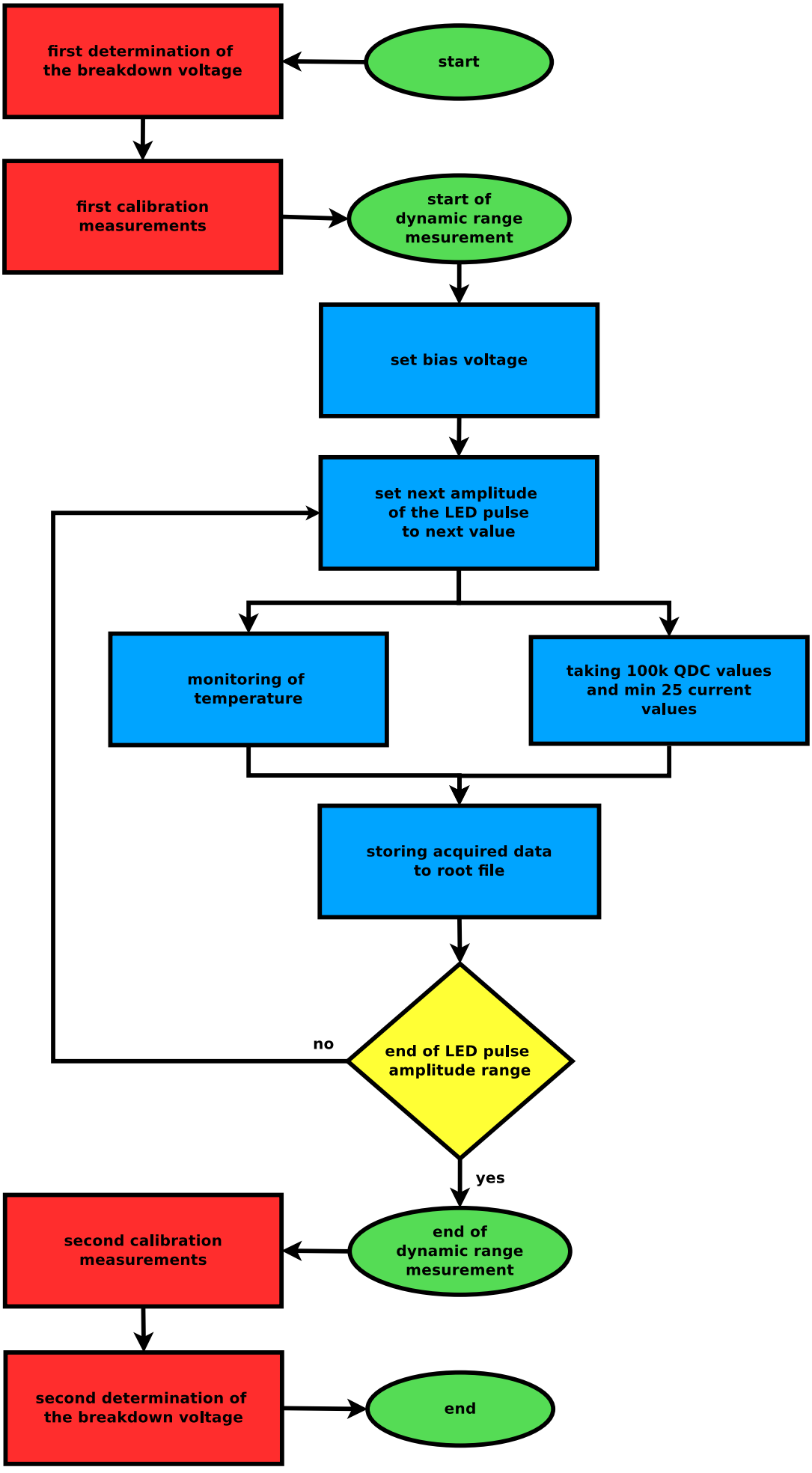

Figure 3.6: Flowchart of the measurment procedure.

Once the original setup is restored, a dynamic range measurement can be performed. It starts with the adjustment of the bias voltage continued by a loop over the LED pulse amplitude range. The LED pulser was adjusted and switched on with a pulse frequency of 5 MHz. After one second sleep time the current values are recorded. The sleep time is important so that the LED can be adjusted to the new pulses. The frequency is chosen to gain high current values with a small error. Then the frequency is set to 10 kHz and after a sleep time of again one second, the readout of 100k QDC values starts. To determine the gain the LED pulse amplitude is set to 1.8 V. At this voltage, a spectrum, in which the individual peak are easily distinguishable, can be recorded. Plotted into a histogram with a logarithmic ordinate, the spectra looks like fingers and is refereed to as finger spectrum. If no cell fires during the gate, the baseline signal is counted by a peak called pedestal. If one cell fires, a second peak called one photon equivalent peak (1 p.e. peak) occurs etcetera. So each peak represents a specific number of triggered cells. To determine the gain, both, pedestal peak and 1 p.e. peak are fitted by two Gaussian functions. The difference between the two mean values represents the gain. The temperature is monitored to verify later that the breakdown voltage was constant during a measurement. Now the next LED pulse amplitude is adjusted and the loop continues until the end of range LED pulse amplitude range is reached.

After the dynamic range measurement the breakdown voltage and the calibration factor are determined once again to compensate possible variations. During a measurement the temperature is assumed to be constant because temperature variations are smaller than the accuracy of the temperature sensor.

Chapter 4

Analysis

After the previous chapter introduced the measurement procedure, the analysis procedure is outlined in this chapter. It begins with the determination of the breakdown voltage followed by calibration analysis. The next section concentrates on the analysis of the SiPM response measured by both the QDC and the oscilloscope. It gives information on the method used to determine the incoming and detected photon flux. The analysis is done by a self written C++ program and has recourse to the ROOT package developed at CERN. Another section is dedicated to the noise phenomena of the characterised SiPMs. Finally the measurements are compared to simulations made with G4SiPM, a Monte-Carlo framework written at III. Physikalisches Institut A, RWTH Aachen.

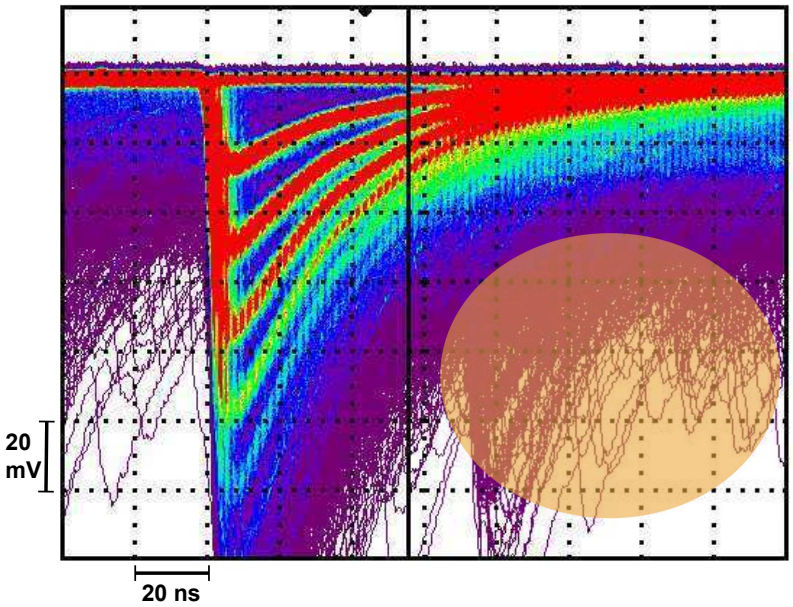

Figure 4.1: Amplified SiPM ($1 \times 1\,\mathrm{mm}^2$; $100\,\mu$m pixel size) signal corresponding to the finger-spectrum in figure 4.2 on page 27. The rate of cell breakdowns decreases from red over green to violet. The shaded area corresponds to afterpulses with a time constant of about 80 ns. (1 division $\widehat{=}$ 20 mV or 20 ns)

4.1 Charge Spectrum

The amplified response of the SiPM can be monitored by an oscilloscope. An oscillogram is shown in figure 4.1. The LED flashes at $t \lesssim 0\,\text{ns}$. A single pulse has a length of $t_{\text{pulse}} = 6\,\text{ns}$. The time shift between LED pulse and SiPM response has not been measured with the used setup and forms an irrelevant value for further analysis. It is caused by the delay between rising edge of the LED pulse and the LED flash and more important by the delay attributed to the amplifier. In the oscillogram, the time of the first breakdown is set to $t = 0\,\text{ns}$. The more cells fire the greater is the delay compared to one fired cell. This is caused by the rise time of the amplifier and the bandwidth of electronic devices. This effect has to be taken into account by the choice of the measurement gate of the QDC. As can be seen in figure 4.2, there are still baseline events where no cell fired. Although there are more events in the baseline as in the first photon equivalent peak, the baseline is more narrow due to signal quality. In a histogram this can be concluded by comparing the width of the pedestal and the photon peaks. The intensity is colour coded and increases from violet over green to red. The shaded area shows possible afterpulses with a time constant of approximately $\tau \approx 80\,\text{ns}$. For this SiPM type a long time constant of $\tau_{\text{long}} = (88.4 \pm 2.6)\,\text{ns}$ has been measured in. A second time constant τ_{short} exists, but is superimposed by the signal [23].

For further analysis, the SiPM response is readout by a Caen V965 QDC. Before the 100k QDC values can be drawn up in a histogram, each QDC value has to be corrected by the pedestal. The pedestal position is thereby set to 0 pC as can be seen in figure 4.2. To determine the precise position of the peaks, Gaussian functions are fitted to the peaks. Only the pedestal peak and the one-photon-equivalent peak are of importance for further analysis. By calculating the difference between the pedestal peak and the one-photon-equivalent peak, the gain is obtained. Another important value is the charge dropped by one LED pulse at average. Dividing this mean charge by the gain one gets the number of fired cells. This is only feasible after all values are corrected by the pedestal. The uncertainty on the gain and on the mean charge have influence on the uncertainty of fired cells. Since the uncertainty on the mean charge drops with $1/\sqrt{N}$. So it is negligibly compared to the error on the gain. The uncertainty on the gain is calculated analogously. As introduced in the previous chapter, the gain is determined at each single amplitude of the LED pulse. So its uncertainty is given by the RMS calculated of all gain values.

4.2 Breakdown Voltage

To determine the breakdown voltage, six QDC spectra are taken at six different bias voltages. Per definition the breakdown voltage corresponds to the bias voltage at which the gain equals zero. With increasing bias voltages the gain and the dropped charge rises linearly. Therefore a custom peakfinder algorithm was used to find the peak position of the pedestal and the one-photon-equivalent. Due to the fact that both peaks start to merge into each other with decreasing bias voltage, the algorithm is only applicable on spectra taken with an overvoltage $V_{\text{over}} \geq 1\,\text{V}$.

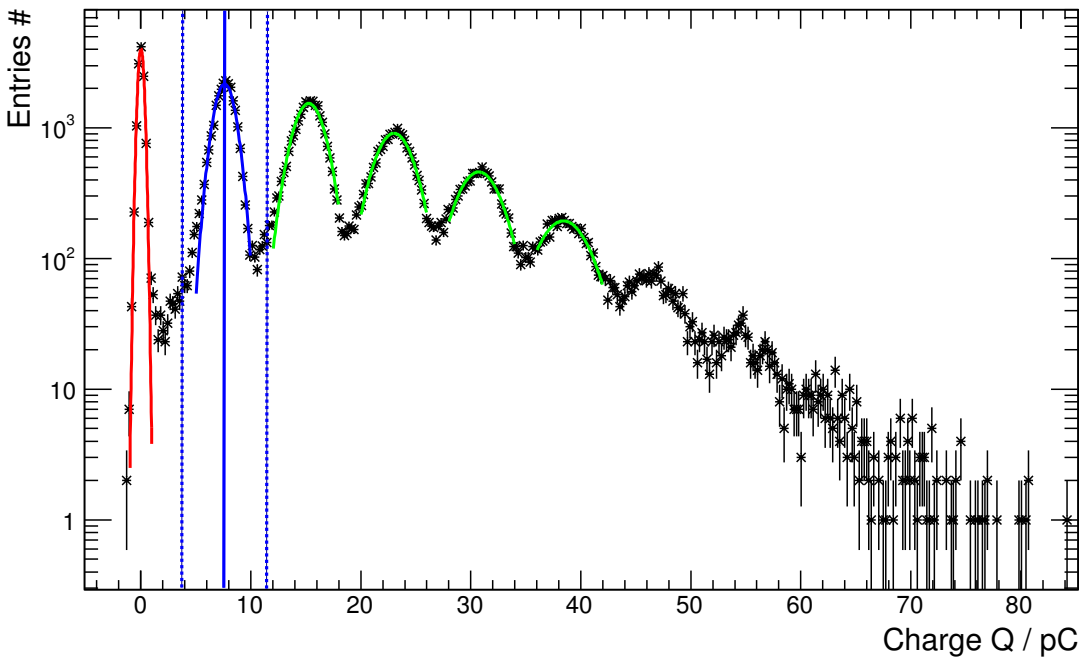

Figure 4.2: Finger spectra of an SiPM with 400 cells ($1 \times 1\,\mathrm{mm}^2$; $100\,\mu$m pixel size) taken for calibration measurement containing 100k QDC values. Peaks are fitted with Gaussian functions. All entries within the dotted area count to the one photon equivalent peak. The straight line represents the peak position of the 1 p.e. peak. It is the corresponding histogram to the oscillogram shown in figure 4.1 on page 25.

Type: S10361-	V_{break} [V]	V_{bias} [V]	V_{over} [V]	Temperature T [°C]
11-100C	69.11 ± 0.004	69.60 ± 0.01	0.49 ± 0.01	25.4 ± 0.1
11-400C A	69.88 ± 0.004	70.20 ± 0.01	0.32 ± 0.01	25.8 ± 0.1
11-400C B	69.83 ± 0.003	70.15 ± 0.01	0.32 ± 0.01	25.9 ± 0.1
11-400C C	69.81 ± 0.004	70.15 ± 0.01	0.34 ± 0.01	25.6 ± 0.1

Table 4.1: Breakdown voltages and temperatures of the characterised SiPMs. V_{break} is the mean value from breakdown voltage measurement before and after the main measurement. Measurements using the 11-400C SiPM were performed three times as explained in section 4.5, so three breakdown voltages are determined. Two different SiPMs of the 11-400C type were used which constitute a higher breakdown voltage in A.

Since the bias voltage can be set in steps of 0.05 V, its uniform distributed uncertainty is given by $\sigma_{V_{bias}} = \frac{0.05}{\sqrt{12}} V$. Now gain is plotted versus bias voltage V_{bias} as shown in figure 4.3. After a linear regression, the breakdown voltage can be extrapolated to a gain of zero. Since the data points almost shape a perfect

straight line, the breakdown voltage can be determined with an uncertainty less than $\sigma_{V_{break}} < 10^{-3} \cdot V_{break}$. Table 4.1 shows the breakdown voltages of the SiPM used in this thesis. The operating overvoltage is given by the difference between applied bias voltage and breakdown voltage. The overvoltage is important for main measurements because its direct proportional to the gain of the SiPM. The breakdown voltage and so the overvoltage is not a constant at all. Both V_{break} and V_{over} decreases with rising temperature. Since the root mean square of all taken temperature values is smaller than the accuracy of the temperature sensor, this effect has not to be taken into account for the measurements performed in this thesis. So the internal bias voltage correction of the amplifier was switched off.

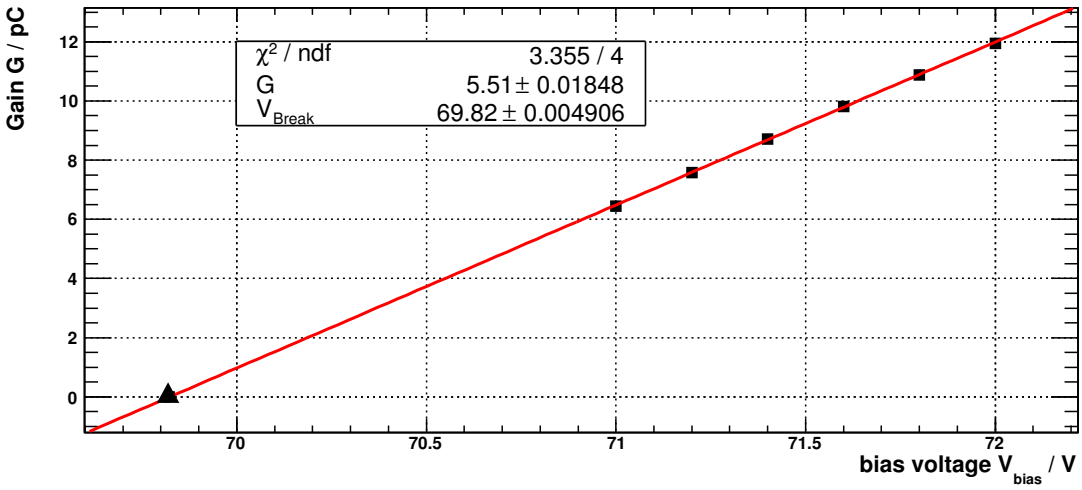

Figure 4.3: Linear regression for determination of breakdown voltage. The quadratic points represent measured values and the triangle represents the extrapolated breakdown voltage. Since pedestal and one-photon-equivalent peak merge into each other for small overvoltages, the gain is only measured at bias voltages $V_{bias} \geq 71\,\mathrm{V}$, so that the peakfinder package is able to distinguish the peaks.

4.3 Calibration of PIN diode

The calibration factor R is needed to convert current of the PIN diode into number of photons irradiating the SiPM. Three effects has to be taken into account. Firstly the differing active area of both sensors and secondarily the quantum efficiencies of both SiPM and PIN diode. The different flux due to the damping of a neutral density filter represents the third factor. Since the factors are either given by manufacturers or are measured, a rough estimate of the calibration factor R_{theo} can be obtained. This enables a comparison to the measured calibration R. The rough estimate is provided by the formula

$$R_{theo} = \frac{A_{\mathrm{PIN,\,active}}}{A_{\mathrm{SiPM,\,total}} \cdot \epsilon_{\mathrm{geom}}} \cdot \frac{QE_{\mathrm{PIN}}}{QE_{\mathrm{SiPM}}} \cdot \frac{1}{DF} \,. \tag{4.1}$$

$A_{\mathrm{SiPM,\,total}}$ is the total area of the SiPM, ϵ_{geom} the geometrical fill factor varying for different SiPM types and $A_{\mathrm{PIN,\,active}}$ represents the active area of the PIN diode. QE_{PIN} and QE_{SiPM} are the quantum efficiencies of PIN diode and SiPM. The damping factor DF is given by the manufacturer at $\lambda = 633\,\mathrm{nm}$. Using the density filters for damping light with $\lambda = 420\,\mathrm{nm}$, DF changes only marginally which was proved within this thesis. The measured calibration factor R, which is used for further analysis, is given by

$$R = R_{\mathrm{measured}} = \frac{I}{I_{\mathrm{Aperture}}} \cdot \frac{Q_{\mathrm{Aperture}}}{Q}. \tag{4.2}$$

If the current of a fully illuminated PIN diode is divided by the current of the PIN diode with the aperture in front, the ratio between the current measured during main measurements and the current generated by illumination of a well-defined area is obtained. Since the aperture ensures that both PIN diode and SiPM see exactly the same number of photons[2], multiplying this ratio with the charge Q_{Aperture} dropped by the SiPM with the aperture in front enables to convert a current I into number of photons hitting the illuminated area of the SiPM. A further division by the charge Q dropped by the SiPM without an aperture provides the sought calibration factor. The following table shows the R values used for further analysis as well as the theoretical factor. As table 4.2 depicts, theoretical and measured values for the correction factors are consistent.

Type: S10361-	$A_{\mathrm{SiPM,\,total}}$	ϵ_{geom}	DF	R_{theo}	R
11-100C	$1\,\mathrm{mm}^2$	78.5 %	$10^{-1.3}$	280	110.4 ± 1.2
11-400C	$1\,\mathrm{mm}^2$	61.5 %	$10^{-0.3}$	30	12.8 ± 0.7

Table 4.2: The table shows the values used to estimate a theoretical calibration factor R_{theo} and the measured value of R. The active area of the PIN diode is given by $A_{\mathrm{PIN,\,active}} = 13\,\mathrm{mm}^2$. The rough estimate shows an additional factor of $c \approx 2.4$ with unknown origin. Nevertheless further analysis are performed with R which is the correct calibration factor for the performed measurements.

4.4 Noise Phenomena

For a later comparison to the simulation, the noise phenomena of the SiPM have to be determined. The simulation package needs a property file containing information on thermal noise, crosstalk and afterpulse probability. Because the gate has only a width of $t_{\mathrm{gate}} = 30\,\mathrm{ns}$ or $t_{\mathrm{gate}} = 45\,\mathrm{ns}$ the afterpulse probability P_{ap} is not determinable out of the recorded data. The values listed in table 4.3 are extrapolated values from [23].

[2]The neutral density filter was mounted in front of both SiPM measurements and PIN diode with the aperture in front.

4.4.1 Thermal Noise

The data of the main measurement contains four QDC spectra with a non-illuminated SiPM. These data can be used to calculate the thermal noise. In a histogram like the one shown in figure 4.2 the entries $N_{\text{1p.e.}}$ corresponding to the one-photon-equivalent peak are counted. Assuming that the width of a photon-equivalent peak equals the gain, all entries in the interval of the width of the gain belongs to a specific photon-equivalent peak. This is exemplary shown in figure 4.2 for the one-photon-equivalent peak. Here the interval ranges from 0.5 p.e. to 1.5 p.e.. Now the thermal noise rate can be calculated using the formula

$$f_{\text{thermal}} = \frac{N_{\text{1p.e.}}}{N_{\text{total}}} \cdot \frac{1}{t_{\text{gate}}} \ . \tag{4.3}$$

N_{total} is the number of total QDC values and t_{gate} the width of the gate. The results are shown in table 4.3. Care has to be taken because thermal noise rates are overvoltage and temperature dependant and can vary from SiPM to SiPM. So only a dimension comparison with values given by the manufacturer or other measurements can be made.

4.4.2 Optical Crosstalk

The crosstalk probability P_{ct} can be extracted out of the same data used for the thermal noise rate. If a cell fired on the effect of thermal noise it is possible that exactly one cell fires due to crosstalk. Since the thermal noise rates are small enough compared to crosstalk probabilities, the probability that two cells fires during the gate due to thermal noise is very low. Hence all entries in the two-photons-equivalent peak are attributed to crosstalk. A cell triggered by crosstalk can itself produce an photon too which leads to another firing cell which will lead to an entry in the three-photons-equivalent peak. So the crosstalk probability can be calculated via

$$P_{\text{ct}} = \frac{N_{\text{2p.e.}}}{N_{\text{1p.e.}}} \cdot \kappa \ . \tag{4.4}$$

The factor κ arises due to the fact that edge cells have less neighbours than cells in the center of the SiPM which result in a smaller crosstalk probability for edge cells. As a consequence the measured crosstalk probability $P_{\text{ct, measured}}$ has to be corrected by a factor κ to compensate this effect. Determination and values of κ can be found in [24].

Type: S10361-	f_{thermal}	P_{ct}	P_{ap}	τ_{recover}	κ
11-100C	(568 ± 40) kHz	(6.5 ± 1.6) %	$\approx 10\%$	(41.1 ± 4.0) ns	1.170
11-400C	(377 ± 27) kHz	(6.6 ± 2.2) %	$\approx 5\%$	(13.8 ± 2.5) ns	1.080

Table 4.3: Measured specifications are valid for the SiPMs characterised in this thesis. They depends on temperature and strongly on the overvoltage. Afterpulse probabilities and recovery times was taken from [23]. The crosstalk correction factor κ is of geometrical origin and was adapted from [24].

Crosstalk probabilities measured at higher overvoltages can be found in [23]. Except the recovery time, table 4.3 shows the probabilities calculated out of taken data. So the values are specific for the used SiPM. The recovery time and noise phenomena as a function of the overvoltage can be found in [23].

4.5 Dynamic Range

The acquirements of the first section of this chapter enable to calculate the effective number of fired cells out of charge dropped by SiPMs. The third section of the previous and this chapter explain how to get the number of photons irradiating the SiPM. Plotted both in a graph, a comparison between input and output at different light fluxes is possible. A graph of such a dynamic range of an SiPM with 100 cells ($1 \times 1\,\text{mm}^2$; $100\,\mu$m pixel size) is shown in figure 4.4. The measurement was performed at an overvoltage of $V_{\text{over}} = (0.49 \pm 0.04)\,\text{V}$. Since a cell is able to fire without being fully charged, the ordinate plot the effective number of fired cells. So two semi-charged cells count as one effectively charged cell. At low fluxes (< 250 photons) the response is nearly proportional to the incoming flux because the probability that two photons hit different cells exceeds the one that two photons hit the same cell. A linear regression yields to a photon detection efficiency of $PDE = (18.1 \pm 0.3)\,\%$. A photon detection efficiency of $PDE \approx 16\,\%$ can be extrapolated out of data taken in [23]. Here the correlated noise effects were excluded. With increasing fluxes, the frequency that two photons irradiating on one cell is rising. As a result, the effective number of fired cells $N_{\text{fired, eff}}$ begins to saturate exponentially. Figure 4.5 shows a zoomed graph of the linear range. As can be see there is no offset which is important for the determination of the beginning of the dynamic range.

For an ideal SiPM[3] the maximal number of fired cells N_{max} is given by the number of cells N_{total} the SiPM consists of. If an instantaneous light pulse and QDC readout is used, the following formula[4] allows to calculate the number of fired cells N_{fired} as a function of the number of photons N hitting the SiPM, the PDE and N_{total} for an ideal SiPM:

$$N_{\text{fired}} = N_{\text{total}} \cdot \left(1 - \exp\left(-\frac{PDE \cdot N}{N_{\text{total}}}\right)\right) \tag{4.5}$$

[3] without any noise phenomena including thermal noise, crosstalk and afterpulses

[4] taken from [14]

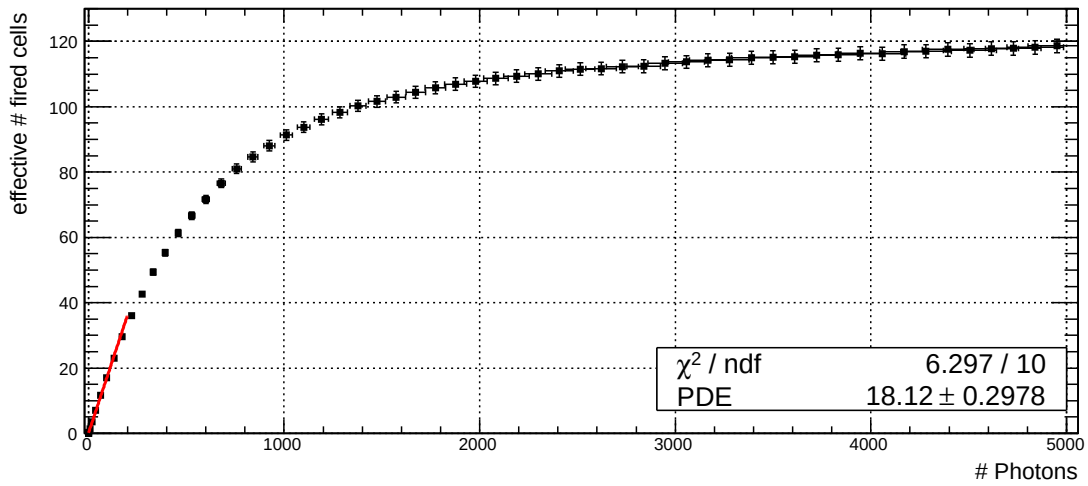

Figure 4.4: Dynamic range of an SiPM with 100 cells ($1 \times 1\,\mathrm{mm}^2$; $100\,\mu$m pixel size) at an overvoltage $V_{\mathrm{over}} = (0.49 \pm 0.04)\,\mathrm{V}$. At low fluxes ($N_{\mathrm{fired,\ eff}} \lesssim \frac{1}{3} N_{\mathrm{total}}$) the response is nearly proportional to the incoming flux. The constant of proportionality is given by the photon detection efficiency $PDE = (18.1 \pm 0.3)\,\%$ (noise phenomena included). At higher fluxes $N_{\mathrm{fired,eff}}$ starts to saturate exponentially. Since an extensive light flash was used and the gate of the QDC amounts to 30 ns, one cell may fire a second time (Recovery times are shown in table 4.3 on page **??**).

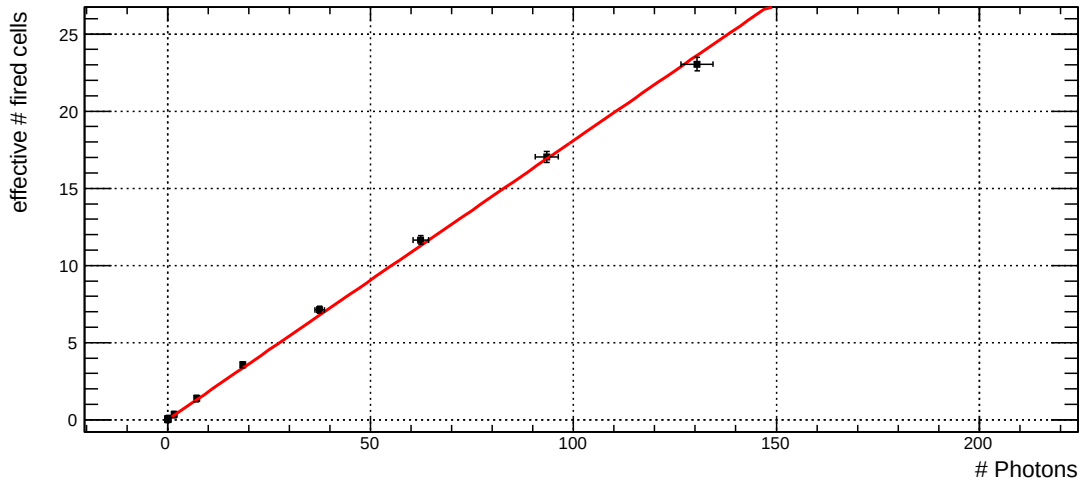

Figure 4.5: Zoom of figure 4.4 into the low photon flux area of the dynamic range of an SiPM with 100 cells ($1 \times 1\,\mathrm{mm}^2$; $100\,\mu$m pixel size). Both, irradiating and measured photon fluxes have an offset of zero.

In reality the model of an ideal SiPM is untenable due to noise phenomena. Since a cell is triggered by an incoming photon or due to noise phenomena, the exponential dependency is only valid for first approximation. Additionally the light pulse as well

as the gate have a finite length of time, with the result that $N_{\text{max}} \gtrsim N_{\text{total}}$. As can be seen in the plot, the theoretical saturation is superimposed by a slight growth. This is attributed by cells firing a second time without being fully charged. For this reason the function is not applied here on the data, but in the next section on the simulated data without noise phenomena.

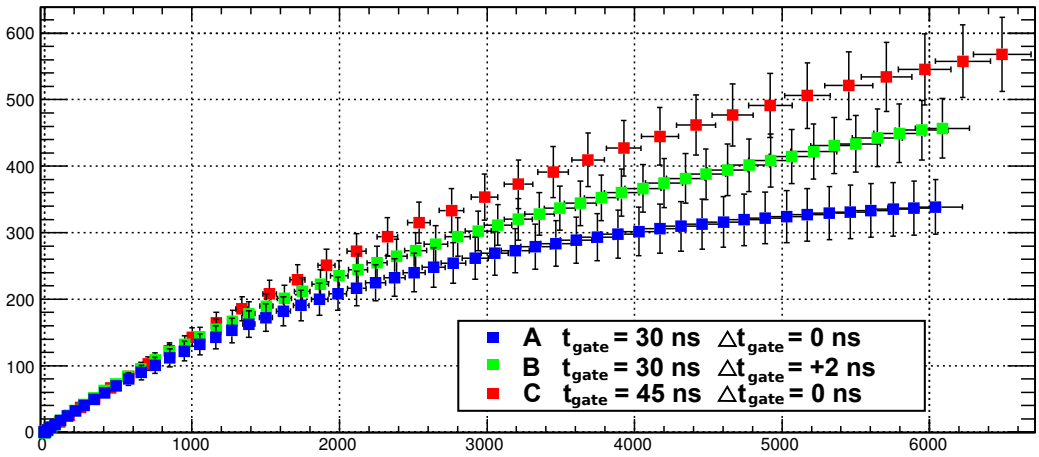

Figure 4.6: Dynamic range of an SiPM with 400 cells ($1 \times 1\,\text{mm}^2$; $50\,\mu$m pixel size) at $V_{\text{over}} \approx 0.3\,\text{V}$ as can be extracted from table **??**. The discrepancy at higher fluxes is caused by amplifier effects.

The effect of shifting minima of the SiPM response does not become apparent in measurements with 11-100C SiPM. So the effective number of fired cells is independent from gate length and from varying the gate position in a small interval. Analysing the data of 11-400C SiPM, shows the opposite, as can be seen in figure 4.6. The blue quadratic data points represent the first measurement with this SiPM type. Because the saturation value is smaller than the total number of SiPM cells N_{total}, the assumption was made that there are maybe some broken cells. But with the discovery of the shifting minima effect, this assumption was discarded after measurements with another SiPM of the 11-400C type. So three different gate times were chosen. The first (blue data points) was exactly the same as used for the 11-100C SiPM. Using the initial gate leads the QDC not to integrate over the whole minimum position of the SiPM response at high fluxes. Effectively the QDC "sees" more of the baseline because the minimum drifts out of the gate. Since the optimal position is not exactly justifiable out of an oscillogram an assumed shift of $\Delta t = +3\,\text{ns}$ was chosen (green data points). Trying to compensate this effect and the fact that an optimal position is not justifiable a third gate with a total $t_{\text{gate}} = 45\,\text{ns}$ was chosen. It was not time shifted compared to the initial gate (blue points). But now another effect emerges. The tail of the amplified SiPM response is not proportional to the fired cells anymore, because it decays slower than the original SiPM response. As a result the measured charge is overestimated, which results in a maximal number of fired cell $N_{\text{max}} > N_{\text{total}}$. The real data points should lie somewhere between the

blue and the red data points and might match the green points. But this was not provable during this bachelor thesis.

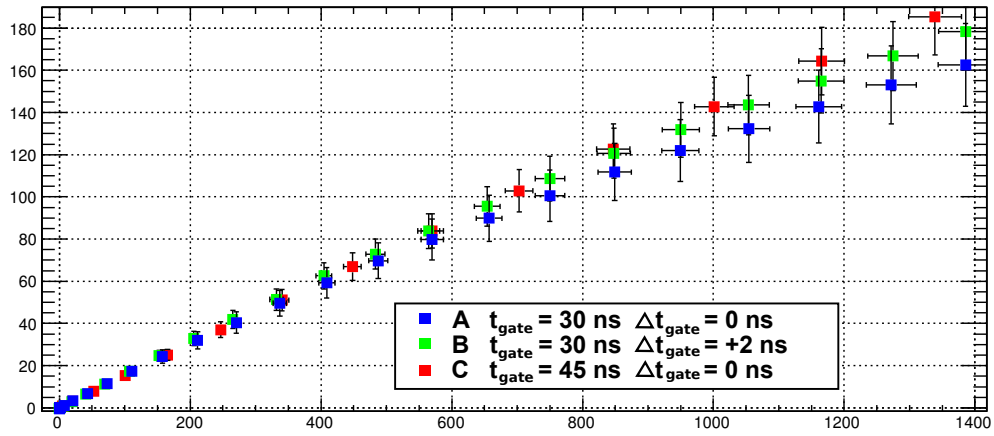

Figure 4.7: Zoom into the low flux area of the dynamic range plot of an SiPM with 400 cells ($1 \times 1\,\mathrm{mm}^2$; $50\,\mu$m pixel size) shows the linear range ($N_{\text{fired, eff}} \lesssim \frac{1}{3} N_{\text{total}}$). The measurements agree within the uncertainties, but a systematic shift due to amplifier effects become already apparent.

Since the lastly discussed effects appears only at higher fluxes, the domain of low fluxes coincides within the uncertainties, as can be seen in figure 4.7. The consistency of the data verifies the assumption that the amplifier distorts the detected photons at high fluxes. The larger uncertainties compared to the ones in the 11-100C SiPM plot arise from the smaller gain. A smaller gain results in a larger uncertainty because the peaks being merging into each other. Additionally the smaller the gain and the more both peaks overlap, the more the gain is underestimated. The peak position of the pedestal is overestimated and the peak position of the 1p.e. peak is underestimated. As a result of the underestimated gain, the PDE rises to about $PDE \approx (13 \pm 2)\,\%$ despite the lower applied overvoltage compared to the measurements with the 11-100C SiPM.

The dynamic range is defined as the range providing a precise calculation of the photon flux irradiating the SiPM out of the measured photon flux. Due to the fact that both fluxes have an offset of zero, the beginning of the dynamic range of the two characterised SiPMs is given by a photon flux of zero. The end of the dynamic range is reached when the measured photon flux is compatible with the saturation value N_{max} within the uncertainties. To calculate N_{max} the exponential saturation function 4.5 is fitted on the data. Although the function can not reproduce the exact behaviour, the function can be used to estimate N_{max}. Since the theoretical saturation is not reached due to additional cell triggers with not fully loaded cells, it is only possible to calculate an estimator of N_{max}. For the 11-100C SiPM, the saturation values has been determined to $N_{\text{max}} \approx 110$. The error on a single value is given approximately by $\sigma \approx \pm 4$ cells. So the end of the dynamic range of the 11-

100C SiPM with a gate of $t_{\text{gate}} = 30\,\text{ns}$ is reached at approximately 1500 photons. The end of the dynamic range of an 11-400C SiPM is only rough determinable due to the large uncertainties on the measured values. The saturation value is very roughly determinable as $N_{\text{max}} \approx 500 \pm 100$ which yields to an end of the dynamic range to a photon flux of about 1000 to 2000 photons.

4.6 Comparison to G4SiPM

The G4SiPM simulation package enables to illuminate an virtual SiPM with a defined flux of photons. It provides setting an incident angle range, an energy range of the photons and the duration of illumination. To simulate the SiPM response, the simulation package needs a property file containing information about the photon detection efficiency, correlated noise, the thermal noise rate and recovery times of cells. Providing all these data a simulation of a specific flux can be performed. The resulting data are itemised by triggered cell number, trigger timestamp, and the reason of triggering (detected photon, crosstalk, afterpulse or thermally triggered). Additionally the simulation calculate the cell gain recovery, corresponding to whether a cell was fully or less loaded before triggering.

Simulation was only performed for the 11-100C SiPM due to the uncertainties of the 11-400C SiPM. To increase the statistics and to estimate an uncertainty on the simulated data, 200 simulations of each N value was performed. The noise analysis of section 4.4 was used to provide the required quantities to fill the property file. Additionally, the PDE determined in section 4.5 has to be noise corrected which was executed iteratively. Therefore, a simulation with the uncorrected PDE was performed. The resulting data distinguishes between signal and the different noise phenomena. Fitting the function 4.5 on the signal data, yields in a first approximation noise corrected photon detection efficiency of $PDE_{\text{corr}} = 15.5\,\%$. Afterwards a second simulation with the new PDE_{corr} was performed. The simulated data are plotted with the measured data in upper graph of figure 4.8.

The plot contains the measured data as well as the simulated data. Since the G4SiPM simulation package is able to distinguish between the possible trigger causes (signal, crosstalk, afterpulses and thermal noise), the cleaned photon signal is plotted additionally. As a consequence, the function 4.5 is fitted on the clean signal. Of course N_{max} exceeds negligible the total number of SiPM cells N_{total} due to a LED pulse length of $t_{\text{pulse}} = 6\,\text{ns}$. The obtained photon detection efficiency $PDE_{\text{ideal}} = (12.9 \pm 0.4)\,\%$ represents the probability that an incoming photon triggers a cell for an ideal SiPM without correlated noise. Hence the ideal PDE is smaller than the measured PDE ($PDE_{\text{ideal}} < PDE_{\text{measured}}$). In the bottom part of figure 4.8, simulated values minus measured data are plotted. The number of effectively fired cells of the simulation is always smaller the the measured values. Within this bachelor thesis, a plausible explanation could not be found because it is unknown if this spread arises from amplifier effects or a non-conforming assumption while carrying out the simulations.

As explained in chapter two, an SiPM can be represented by a capacity and a resistor in an equivalent circuit diagram. As a consequence the applied overvoltage recovers

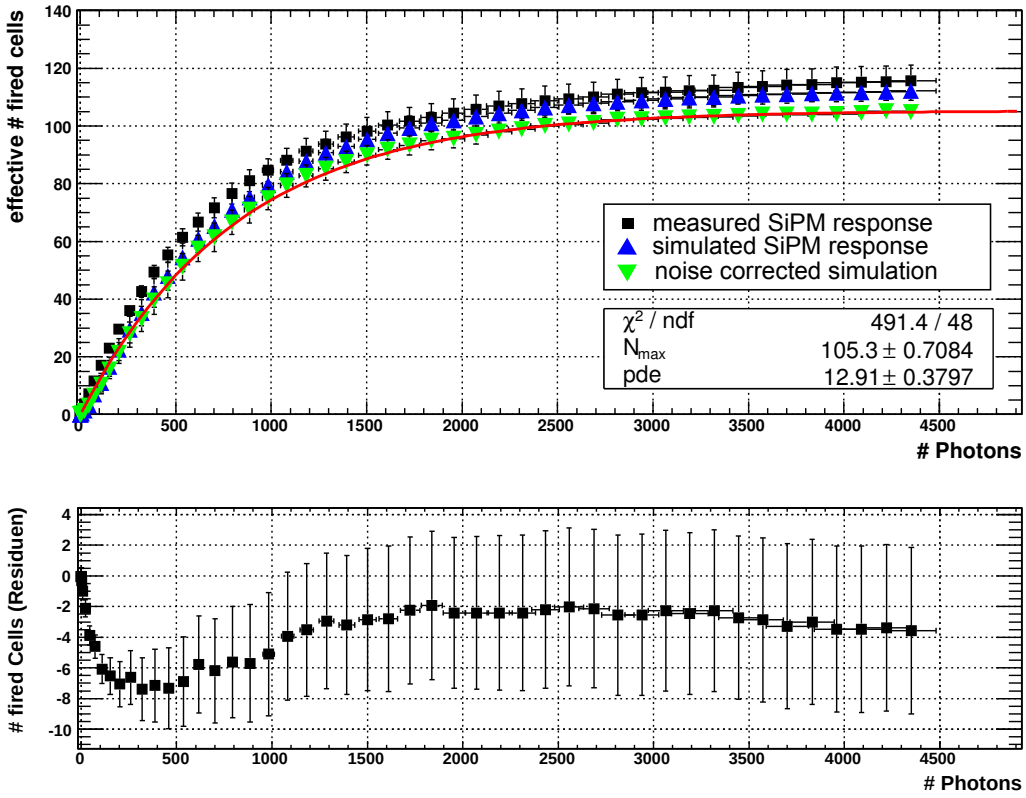

Figure 4.8: Top: Simulated dynamic range of an SiPM ($1 \times 1\,\mathrm{mm}^2$; $50\,\mu$m pixel size). For comparison, the black quadratic points show the measured dynamic range of figure 4.4. The simulated SiPM response is represented by blue triangles. The upside down green triangles depict the correlated noise corrected simulated signal and are fitted by the function 4.5. N_{max} exceeds the total number of cells in the SiPM, because a single cell can multiple fires during the gate of $t_{\mathrm{gate}} = 30\,\mathrm{ns}$. Bottom: residuum plotted simulated data minus measured data (black quadratic points minus blue triangles).

exponentially as well as the gain which is proportional to the overvoltage. Since the simulation package calculate this recovery status of a cell, the recovery status can be histogrammed for different photon fluxes. Histograms with three different number of photons (50, 500 and 5000) illuminating the SiPM can be found in figure 4.9. The values are averaged over 5000 single simulation with the specific photon flux. For a photon flux of 50 photons per pulse, approximately 95 % of the cells are fully loaded before a cell trigger. If the SiPM is irradiated with 500 photons per pulse, more than 10 % of the fired cells are less than 20 % loaded. At a photon flux of 5000 photons per pulse, the number of low loaded cells exceed the number of fully loaded cells by a factor of ten. This is the reason why the term ”effective number of fired cells” is used in the dynamic range section.

Within this thesis and with the used devices, the dynamic range of 11-100C SiPM has been determined to range from 0 to 1000 photons per pulse. The pulse length

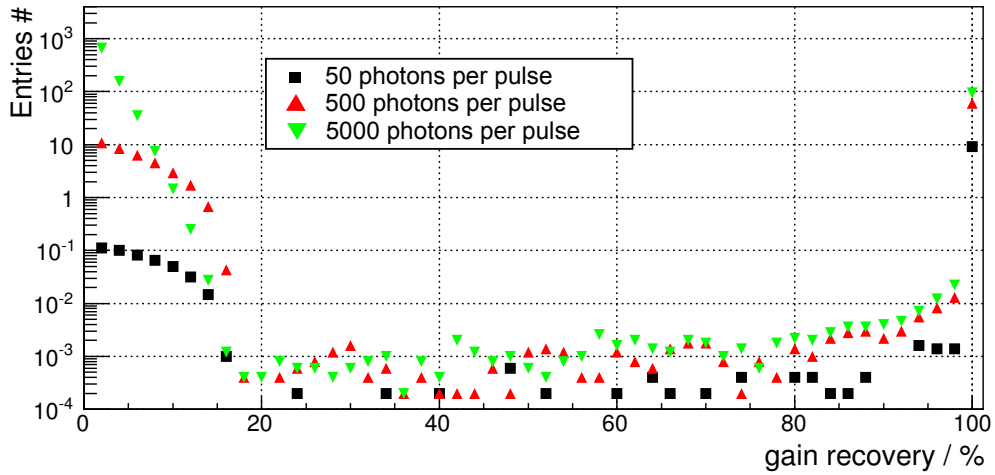

Figure 4.9: Histogram of simulated recovery status of a triggered cell. Correlate noise has been excluded. The effective number of triggered cells is mainly given by cell triggers which were fully loaded before a breakdown. At a photon flux of 5000 photons per pulse, the real number of triggered cells exceeds the number of effective number of fired cells by a factor of ten.

was $t_{\text{pulse}} = 6\,\text{ns}$, the overvoltage has been determined to $V_{\text{over}} = (0.49 \pm 0.01)\,\text{V}$ at an ambient temperature of $T = (25.4 \pm 0.1)\,°\text{C}$. The simulated dynamic range is compatible within the uncertainties. Nevertheless there is a systematic shift exists, but a plausible reason could not be found within this thesis. Characterising the dynamic range of 11-400C SiPM proved difficult due to amplifier effects. As a consequence no simulation have been carried out. The dynamic range has to be taken with care. The end of the dynamic range could be estimated to be between 1000 and 2000 photons per pulse. Here, too, the pulse length was $t_{\text{pulse}} = 6\,\text{ns}$. The mean overvoltage of the three measurements has been determined to $V_{\text{over, mean}} = (0.32 \pm 0.01)\,\text{V}$ at an ambient temperature of $T = (25.8 \pm 0.1)\,°\text{C}$.

Chapter 5

Summary and Outlook

A branch of current research of cosmic rays is dealing with **u**ltra **h**igh **e**nergetic **c**omic **r**ays (UHECRs). Due to the very low flux of these UHECRs, large and very efficient ground based detectors are needed to investigate them, which is done for instance at the Pierre Auger Observatory. The "**F**irst **A**uger **M**ulti-pixel-photon-counter-camera for the **O**bservation of **U**ltra-high-energy-cosmic-ray air **S**howers" (FAMOUS) may be a more efficient successor of the present used fluorescence telescopes based on photomultiplier tubes as light sensitive component.

Since novel **si**licon **p**hoto**m**ultipliers (SiPMs) are applied in FAMOUS, many characterisation studies have been performed in recent time. This thesis aimed to characterise the dynamic range of two SiPMs out of the S10361 series manufactured by Hamamatsu. A measurement setup was developed allowing to illuminate the SiPMs with well-defined fluxes of light. The dynamic range of an SiPM consisting of 100 cells could be determined successfully and ranges from zero to 1000 photons per pulse. Due to limitations of the used amplifier, it was only possible to determine the dynamic range for overvoltages $V_{\text{over}} \leq 0.5\,\text{V}$. The dynamic range of the second SiPM with 400 cells can only handled with care because here, too, the amplifier has been stretched to its limit and distort signals at high fluxes. A rough end of the dynamic range could be estimated to be between 1000 and 2000 photons per pulse.

Nevertheless, it was proven that responses of both SiPMs are linear within the uncertainties, as long as less than a third of all cells of the SiPM were triggered. Beyond, the linear range begins to saturate exponentially. Furthermore, noise phenomena at low overvoltages were determined successfully which are needed to simulate the dynamic range with G4SiPM. The simulation package G4SiPM bases on Geant4 and has been developed at III. Phyiskalisches Institut A, RWTH Aachen. Simulations of an SiPM with 100 cells are carried out successfully and show that simulated and measured data are consistent within the uncertainties.

At III. Physikalisches Institut A, RWTH Aachen, a new amplifier board is developed. The operation range of this amplifier is enhanced so it will be possible to measure the dynamic range of SiPM consisting of more than 400 cells as well as to perform measurements at an overvoltage of $0.5\,\text{V} \leq V_{\text{over}} \leq 1.3\,\text{V}$. Another important task is to characterise the dynamic range at pulse length greater than 6 ns which will be possible using a amplifier with an enlarged operation range.

A. Appendix

A.1 List of Abbreviations

APD	**A**valanche **P**hoto**d**iode
EAS	**E**xtensive **A**ir **S**hower
eh-pair	**e**lectron **h**ole pair
FAMOUS	**F**irst **A**uger **M**ulti pixel photon counter camera for the **O**bservation of **U**ltra-high-energy cosmic ray **S**howers
G-APD	**A**valanche **P**hoto**d**iode operating in the **G**eiger mode
LHC	**L**arge **H**adron **C**ollider
p.e.	**P**hoton **P**eak
PDE	**P**hoton **D**etection **E**fficiency
PMT	**P**hot**m**ultiplier **T**ube
SiPM	**Si**licon **P**hoto **M**ultiplier
UHECR	**U**ltra-**H**igh **E**nergetic **C**osmic **R**ay

References

[1] " R. A. Mewaldt : Cosmic Rays", available online http://www.srl.caltech.edu/personnel/dick/cos_encyc.html, visited 19.10.2012

[2] " V. F. Hess : Über Beobachtungen der durchdringenden Strahlung bei sieben Freiballonfahrten", Z. Phys., 13(1912), p. 1084

[3] " W. Hanlon : Updated cosmic ray spectrum", available online http://www.physics.utah.edu/ whanlon/spectrum.html, visited 19.10.2012

[4] " III. Physikalisches Institut A, RWTH Aachen : The Optics and Detector-Simulation of the Air Fluorescence Telescope FAMOUS for the Detection of Cosmic Rays", p. 1

[5] " Pierre Auger Observatory", available online http://www.auger.org/cosmic_rays/1938.html, visited 19.10.2012

[6] " Pierre Auger, Roland Maze, Paul Ehrenfest et André Freon : Les grandes gerbes de rayons cosmiques", J. Phys. Radium 10, 39-48 (1939)

[7] " Malcolm S. Longair : High Energy Astrophysics", Third Edition printed in the United Kingdom at the University Press, Cambridge (2011)

[8] " Sonali Bhatnagar : Extensive Air Shower High Energy Cosmic Rays (II) ", Department of Physics & Computer Science Dayalbagh Educational Institute, Agra. (2009)

[9] " Oliver Pooth : Vorlesung Astro- und Teilchenphysik ", III. Physikalisches Institut der RWTH Aachen, WS2011

[10] " Prof. C. Wiebusch : Vorlesung Astro- und Teilchenphysik ", III. Physikalisches Institut, RWTH Aachen, SS2010

[11] " HAWC Collaboration: Detecting Cosmic Rays", availible on the web at http://hawc.umd.edu/science/detection.php, visited 26.10.2012

[12] " Johannes Blümer, Ralph Engel and Jörg Hörandel : Cosmic Rays from the Knee to the Highest Energies ", Karlsruhe Institute of Technology (KIT), Radbound

[13] " Prof. M. Morgenstern : Vorlesung Physik der Kondensierten Materie ", II. Physikalisches Institut B, RWTH Aachen, SS2012

[14] " D. Renker and E. Lorenz : Advances in solid state photon detectors ", published by IOP Publishing for SISSA, 2009

[15] " F. Scheuch : Measurement and simulation of electrical properties of SiPM photon detectors ", master thesis, III. Physikalisches Institut A, RWTH Aachen, Nov 2012

[16] " P. Hallen : Determination of the Recovery Time of Silicon Photomultipliers ", bachelor thesis, III. Physikalisches Institut A, RWTH Aachen, Sep 2011

[17] " T. Niggemann : The Optics and Detector-Simulation of the Air Fluorescence Telescope FAMOUS for the Detection of Cosmic Rays, III. Physikalisches Institut A, RWTH Aachen, 2012

[18] " Datasheet of Hamamatsu SiPM series S10361 "

[19] " Datasheet of Hamamatsu FSD100 Si Photodiode "

[20] " Datasheet of Conrad LED 5004PCH02 ", availible on the web at http://www.produktinfo.conrad.com, visited 16.01.2013

[21] " Datasheet of QDC Caen V965 "

[22] " J. Rennefeld : Studien zur Eignung von Silizium Photomultipliern für den Einsatz im erweiterten CSM Detectos am SLHC ", diploma thesis, III. Physikalisches Institut B, RWTH Aachen, Feb 2010

[23] " M. Lauscher : Characterisation Studies of Silicon Photomultipliers for the Detection of Fluorescence Light from Extensive Air Showers ", master thesis, III. Physikalisches Institut A, RWTH Aachen, Jan 2012

[24] " A. Künsken : Measurements of silicon photomultipliers at different operating points and simulation with GEANT4 ", master thesis, III. Physikalisches Institut A, RWTH Aachen, Nov 2012

Acknowledgements

Danksagungen

Hiermit möchte ich mich bei all denen bedanken, die mir bei der Erstellung dieser Arbeit geholfen haben. Ohne sie wäre das in diesem Umfang und in dieser Ausführlichkeit nicht möglich gewesen.

Ein ganz besonderer Dank gilt Prof. Dr. Thomas Hebbeker. Vielen Dank, dass ich an Ihrem Institut diese Bachelorarbeit verfassen durfte. In zahlreichen Meetings habe ich viel über die Arbeitsweisen eines Physikers gelernt. Wie man physikalische Diskussionen führt und wie man kompetente Präsentationen erstellt.

Weiterhin möchte ich mich bei Tim Niggemann bedanken, der die Betreuung dieser Bachelorarbeit übernommen hat. Er hat mir mehr als nur das für diese Arbeit notwendige Verständnis vermittelt. Bei anfänglichen Schwierigkeiten bei der Programmierung in C++ und Python hat er mir sehr geholfen. Er hatte immer ein offenes Ohr für mich und stand mir bei Problemen und Fragen immer zur Seite. Durch seine fachliche Kompetenz war ein zufriedenstellender Abschluss dieser Arbeit möglich.

Ein weiterer Dank geht an Markus Lauscher, der sich bereit erklärt hat, für die ersten vier Wochen meiner Bachelorarbeit die Betreuung zu übernehmen. Die Bereitschaft für die zusätzliche Arbeit rechne ich ihm sehr hoch an. Er hat mir das Grundverständnis sowohl für die benutzten Geräte als auch für meine späteren Messungen vermittelt.

Danke auch an Maurice Staphan und Lukas Middendorf, die mir beide bei so manchen experimentellen Fragen weiterhelfen konnten. Dank Lukas konnte der Arbeitsbereich des verwendeten Verstärker an die Anforderungen der Bachelorarbeit angepasst werden.

Zudem möchte ich mich bei Marcel Straub bedanken, der mir zu Beginn bei der Programmierung in C++ geholfen hat.

Zuletzt möchte ich mich bei Herrn Zantis und seinem Team bedanken, die mir immer schnell weiter geholfen haben, wenn ich ihre Hilfe benötigte.

Ein abschließender Dank geht an alle Kollegen des III. Instituts A der RWTH Aachen für die schönen gemeinsamen Stunden, die lehrreichen Meetings und ihre Hilfe bei der Erstellung dieser Arbeit.

Erklärung

Hiermit versichere ich, dass ich diese Arbeit einschließlich aller enthaltenen Abbildungen, Graphen und Tabellen eigenständig erstellt habe und keine anderen als, die im Quellenverzeichnis angegebenen Quellen, verwendet habe. Zitate oder Stellen, die dem Wortlaut oder Sinn nach anderer Werke entnommen sind, habe ich als solche deutlich unter Angabe ihrer Quelle gekennzeichnet.

Aachen, den 28. Februar 2013

Tobias Kowalew